



UNIVERSITY OF LEEDS

This is a repository copy of *Quantitative measurement of olivine composition in three dimensions using helical-scan X-ray micro-tomography*.

White Rose Research Online URL for this paper:  
<http://eprints.whiterose.ac.uk/138141/>

Version: Accepted Version

---

**Article:**

Pankhurst, MJ, Vo, NT, Butcher, AR et al. (9 more authors) (2018) Quantitative measurement of olivine composition in three dimensions using helical-scan X-ray micro-tomography. *American Mineralogist*, 103 (11). pp. 1800-1811. ISSN 0003-004X

<https://doi.org/10.2138/am-2018-6419>

---

Copyright © 2018 by the Mineralogical Society of America. This is an author produced version of a paper published in *American Mineralogist*. Uploaded in accordance with the publisher's self-archiving policy. <https://doi.org/10.2138/am-2018-6419>

**Reuse**

Items deposited in White Rose Research Online are protected by copyright, with all rights reserved unless indicated otherwise. They may be downloaded and/or printed for private study, or other acts as permitted by national copyright laws. The publisher or other rights holders may allow further reproduction and re-use of the full text version. This is indicated by the licence information on the White Rose Research Online record for the item.

**Takedown**

If you consider content in White Rose Research Online to be in breach of UK law, please notify us by emailing [eprints@whiterose.ac.uk](mailto:eprints@whiterose.ac.uk) including the URL of the record and the reason for the withdrawal request.



[eprints@whiterose.ac.uk](mailto:eprints@whiterose.ac.uk)  
<https://eprints.whiterose.ac.uk/>

1 **Revision 1**

2 **Title**

3 Quantitative measurement of olivine composition in three dimensions using X-ray  
4 micro-computed tomography.

5

6

7

8 **Authors**

9 Matthew J. Pankhurst<sup>1,2,3,4†</sup>, Nghia T. Vo<sup>5</sup>, Alan R. Butcher<sup>6,7</sup>, Haili Long<sup>6</sup>, Hongchang Wang<sup>7</sup>, Sara Nonni<sup>4</sup>,  
10 Jason Harvey<sup>3</sup>, Guðmundur Guðfinnsson<sup>8</sup>, Ron Fowler<sup>9</sup>, Robert Atwood<sup>4,5</sup>, Richard Walshaw<sup>10</sup>, and Peter D.  
11 Lee<sup>4,11</sup>.

12

13 <sup>1</sup>Instituto Tecnológico y de Energías Renovables (ITER), 38900 Granadilla de Abona, Tenerife, Canary  
14 Islands, Spain.

15 <sup>2</sup>Instituto Volcanológico de Canarias (INVOLCAN), 38400 Puerto de la Cruz, Tenerife, Canary Islands, Spain.

16 <sup>3</sup>School of Earth and Environment, University of Leeds, Leeds, LS2 9JT, UK

17 <sup>4</sup>Research Complex at Harwell, Rutherford Appleton Laboratories, Didcot, OX11 0FA, UK

18 <sup>5</sup>Diamond Light Source Ltd., Didcot, OX11 0DE, UK

19 <sup>6</sup>FEI, Stiklestadveien 1, 7041 Trondheim, Norway

20 <sup>7</sup>Geological Survey of Finland, FI-02151 Espoo, Finland

21 <sup>8</sup>Institute of Earth Sciences, University of Iceland, Reykjavik 101, Iceland

22 <sup>9</sup>Scientific Computing Department, Science and Technology Facilities Council, Rutherford Appleton  
23 Laboratory, Harwell Campus, UK, OX11 0QX

24 <sup>10</sup>Leeds Electron Microscopy and Spectroscopy Centre, University of Leeds, Leeds, LS2 9JT, UK

25 <sup>11</sup>Mechanical Engineering, University College London, Gower Street, London, WC1E 6BT

26 †Corresponding author

27

28

29 **Abstract**

30 Olivine is a key constituent in the silicate Earth; its composition and texture informs petrogenetic  
31 understanding of numerous rock types. Here we develop a quantitative and reproducible method  
32 to measure olivine composition in three dimensions without destructive analysis, meaning full  
33 textural context is maintained. The olivine solid solution between forsterite and fayalite was  
34 measured using a combination of three-dimensional (3D) X-ray imaging techniques, 2D back  
35 scattered electron imaging, and spot-analyses using wavelength dispersive electron probe  
36 microanalysis. The linear attenuation coefficient of natural crystals across a range of forsterite  
37 content from ~73-91 mol% were confirmed to scale linearly with composition using 53, 60 and 70  
38 kV monochromatic beams at I12-JEEP beamline, Diamond Light Source utilising the helical fly-scan  
39 acquisition. A polychromatic X-ray source was used to scan the same crystals, which yielded image  
40 contrast equivalent to measuring the mol% of forsterite with an accuracy <1.0 %. X-ray  
41 tomography can now provide fully integrated textural and chemical analysis of natural samples  
42 containing olivine, which will support 3D and 3D+time petrologic modelling. The study has  
43 revealed >3 mm domains within a large crystal of San Carlos forsterite that vary by ~2 Fo mol%.  
44 This offers a solution to an outstanding question of inter-laboratory standardisation, and also  
45 demonstrates the utility of 3D, non-destructive, chemical measurement. To our knowledge, this  
46 study is the first to describe the application of XMT to quantitative chemical measurement across  
47 a mineral solid solution. Our approach may be expanded to calculate the chemistry of other  
48 mineral systems in 3D, depending upon the number, chemistry and density of end-members.

49

50

51

52

## 53 INTRODUCTION

54 Combining chemical and textural data from rocks is essential to understand their origins and  
55 formation. Integrating these petrologic data means being able to place chemical analyses within  
56 spatial context, and vice versa. Conventional chemical analysis, however, or the preparation for it,  
57 destroys or modifies spatial context in some way. This study documents an advance in non-  
58 destructive, quantitative, determination of composition that maintains full three-dimensional (3D)  
59 context, using olivine.

60 Two-dimensional (2D) data using visible light and electron microscopy has underpinned virtually  
61 all study of rocks at the micro-scale. Quantitative measurement using optical properties of  
62 minerals have been used to investigate rocks for over 150 years (Sorby, 1858). It has also long  
63 been recognised that physical properties, some measurable by optical or X-ray diffraction  
64 analyses, can be used to estimate the chemical composition and vice versa (e.g. Jahanbagloo,  
65 1969; Poldervaart, 1950). In more recent decades, electron microscopy has provided higher  
66 resolution and more analytical options, yet remains limited to 2D measurement. 2D analysis  
67 requires cutting, grinding and polishing of the sample, and thus full spatial context for those  
68 observations is lost. Furthermore, the nature of conventional preparation and analysis is  
69 comparatively slow and expensive, representing a limitation to the gathering of large datasets.

### 70 Motivation and aims

71 The density of olivine can be calculated from its chemical composition and its linear attenuation of  
72 X-rays. It is therefore possible to derive chemical information from X-ray attenuation of olivine.  
73 Pankhurst et al. (2014) showed that X-ray microcomputed tomography (XMT) image brightness  
74 can be used as a proxy for the composition of olivine. Those authors demonstrated equivalence  
75 between electron probe microanalysis (EPMA) and XMT results when comparing population  
76 histograms of olivine core compositions and grayscale number from a split sample of tephra. This  
77 is a viable approach because olivine is generally a solid solution between Fe and Mg end-members  
78 (expressed here as the forsterite content  $Fo = 100 \times Mg/[Mg+Fe+Mn]$ , mineral abbreviations  
79 throughout follow Whitney and Evans, 2010). Yet those results, without calibration, are qualitative  
80 and relative only. Different X-ray beam energies required by different samples, instrument  
81 hardware, environmental conditions and operator choices all contribute to the final image  
82 brightness values. Therefore, without calibration, the brightness values from laboratory source  
83 XMT are arbitrary and non-reproducible.

84 In this study, we test the ability to reliably measure the attenuation of the olivine solid solution in  
85 a volume, using monochromatic XMT, and extract reproducible, quantitative, chemical  
86 information. International standard reference materials (SRMs) are used, as well as other natural  
87 olivine crystals. Our primary aims are to; 1) measure the tomogram image brightness of a range of  
88 olivine compositions using monochromatic X-ray energy; 2) relate those data to density ( $\rho$ ) via the  
89 linear attenuation coefficient ( $\mu$ ); 3) compare results with  $\rho$ , as calculated using EPMA data; 4)  
90 investigate the use of a regression line as a calibration function that employs image brightness as a  
91 quantitative measure of Fo content in a typical laboratory setting (using polychromatic X-rays).

92 First we check that the linear attenuation coefficient ( $\mu$ ) for each value of Fo scales linearly with  
93 Mg-Fe substitution across a Fo range of special interest in nature (i.e., common in mantle and  
94 basaltic rocks), using monochromatic X-ray tomography. We then compare 3D image data from  
95 laboratory (polychromatic) sources, in order to estimate an uncertainty that can be used to  
96 determine the core compositions of large numbers of crystals using scan times of <1 hour. Finally,  
97 we investigate the use of X-ray tomography to provide quantitative 3D chemistry on scales useful  
98 for petrogenetic modelling of crystal margins.

## 99 **Olivine occurrence and importance**

100 Measuring the chemistry of olivine ( $(\text{Mg,Fe})_2\text{SiO}_4$ ) provides insight to its formation, and relationship  
101 with its host rock. Olivine is one of the most important minerals on Earth. It is the most abundant  
102 mineral in the upper mantle and mediates mantle rheology, density, heat flow and melting  
103 (Holtzman et al., 2003; Mizukami et al., 2004). Olivine is also an important component of several  
104 meteorite classes and contain clues as to their evolution (e.g. Rudraswami et al., 2016) as well as  
105 being a rock-forming mineral present in planetary and satellite bodies .

106 Olivine is a rock-forming mineral in ultra-mafic to mafic magmas. It also occurs in some felsic and  
107 hybridised magmas, and can be indicative of mantle-derived magma input to volcanic systems;  
108 frequently implicated as an eruption trigger (e.g. Sigmundsson et al., 2010; Sparks et al., 1977). In  
109 these systems, olivine can occur across a considerable composition range, as well as preserving  
110 major element chemical zonation within individual grains (Kahl et al., 2013). These observations  
111 are leading to new insights as to the origin, dynamics and timescales of magmatic plumbing  
112 systems (Hartley et al., 2016; Pankhurst et al., 2018a). In order to make better sense of these often  
113 highly complex mineralogical records, large datasets that integrate crystal texture and chemistry  
114 are required.

115 The most common substitution in olivine is that between  $2^+$  cations in the M sites. Iron exchange  
116 for Mg is accompanied by a disproportionately large change in the molecular mass of the unit cell  
117 with respect to its volume change (Deer et al., 1992). Accordingly, Fo (Mg end-member:  $\rho = 3.22$ )  
118 is  $\sim 26.5\%$  less dense than fayalite (Fa; Fe end-member:  $\rho = 4.29$ ), which is the property we exploit  
119 here with X-ray imaging. Since electron density is equitable to proton density for a given solid  
120 solution, XMT images of olivine appear much like back-scattered electron (BSE) images, which are  
121 a measure of atomic density (Z contrast). Thus, we can use state-of-the-art 2D BSE imaging as a  
122 useful method of validating the 3D image data.

## 123 **3D data and X-ray microtomography**

124 Full three-dimensional (3D) data from natural samples offers the advantage that measurement of  
125 volume distributions, distances between features and shape descriptors can be conducted  
126 directly. Non-destructive 3D data also has advantages for observing large volumes of material to  
127 find and target rare features, as well as providing context for destructive in-situ measurements.  
128 Obtaining accurate 3D, non-destructive, data from what are (in almost every case) opaque  
129 materials, however, is only possible with tomographic techniques using X-rays, neutrons and  
130 muons (Cnudde and Boone, 2013; Marteau et al., 2012; Winkler et al., 2002).

131 Gathering three dimensional (3D) data at the micro-scale has progressively become more routine  
132 in geological research. Crystallographic orientation and boundary data has traditionally been  
133 obtained from thin sections by using universal stages on petrographic microscopes (see Kile, 2009  
134 for a review). Serial sectioning and well-constrained extrapolation has been used to place  
135 measurements into 3D context across cm scales (Bryon et al., 1995; Cooper and Hunter, 1995). X-  
136 ray computed tomographic imaging (Flannery et al., 1987) provides full 3D data (e.g. Denison and  
137 Carlson, 1997; Philpotts et al., 1999). Centimetre to nanometre resolution X-ray imaging has  
138 become increasingly utilised (Cnudde and Boone, 2013; Ma et al., 2016; Macente et al., 2017;  
139 Suuronen and Sayab, 2018). To date, XMT has been used mainly to recover rock textures (e.g.  
140 Cnudde and Boone, 2013; Fonseca et al., 2013; Jerram et al., 2009; Ketcham, 2005; Mock and  
141 Jerram, 2005), and mineralogy (Lemelle et al., 2004), phase size distributions and their evolution  
142 (Hall et al., 2010; Ketcham and Carlson, 2001; Lin et al., 2016; Reyes et al., 2017), and dynamic  
143 processes such as diffusion through porous rocks (Nakashima, 2000). For a thorough introduction  
144 to XMT applications in geosciences we refer the reader to Cnudde and Boone (2013), and in more

145 detail as applied to igneous texture see (Jerram et al., 2018 and references therein). A key  
146 advantage of XMT is the very high rate of data acquisition that is possible, which can support  
147 efforts to build large datasets efficiently (Pankhurst et al., 2014), and would otherwise rely on  
148 time-intensive analysis.

149 The transmission of X-rays through a rock depends upon minerals' chemistry and density, the  
150 thickness of the sample, and the energy of the X-ray beam. X-rays are attenuated by electrons,  
151 limiting the number of photons arriving at the detector (see Pankhurst et al., 2018b for an  
152 introduction and key references). Contrasts in these properties (and thus electron density)  
153 throughout a sample attenuate an X-ray beam to different degrees, producing differences in  
154 detector response. These responses are recorded as image brightness values.

155 If a reproducible set of beam conditions and settings are used, the values can be directly  
156 compared within and across datasets. For instance, in the case of samples containing one mineral,  
157 if the X-ray energy and linear attenuation coefficient is known, sample thickness can be measured  
158 (Anderson et al., 1998). To map composition in 3D, 2D projections acquired around a sample  
159 (normally the sample is rotated) are tomographically reconstructed; voxel brightness of the  
160 resulting tomographic image can be used to identify different phases (Leber et al., 2004) and the  
161 concentration of certain phases (Yue et al., 2011).

162

## 163 **METHODS**

### 164 **Samples**

165 Samples were selected to provide a useful range of natural occurring olivine at the forsteritic end  
166 of the solid solution ( $\sim\text{Fo}_{70-90}$ ); those compositions dominate olivine occurring in mantle and  
167 basaltic rocks. Intermediate to comparatively evolved olivine ( $\text{Fo}_{30-70}$ ) is less abundant in nature  
168 and could not be obtained in large enough grain sizes; measuring these compositions is planned  
169 for further work at higher resolution. The fayalite end member was nevertheless available. Thus  
170 the sample set contains both a wide spread of compositions, albeit with a higher data density  
171 around the most commonly occurring range  $\text{Fo}_{70-90}$ .

172 Rock samples Killbourne Hole Peridotite (New Mexico, USA), Picrite from Háleyjarbunga lava shield  
173 (Iceland) and an alkali basalt from Papua New Guinea (Star-1) were coarsely crushed. A large ( $\sim 2$   
174 cm) forsterite crystal from the locality of San Carlos, New Mexico, and part of a large ( $\sim 4$  cm) piece  
175 of fayalite from Rockport, Mass (USA), were also coarsely crushed. Olivine was handpicked under a  
176 binocular microscope from the crushed material, and from some tephra samples (flank and  
177 summit samples from the 2010 Eyjafjallajökull) and sand from a green beach from Hawaii (legacy  
178 sample from Papakōlea). We direct the reader to Fig. 1 for a description of how the olivine was  
179 mounted for analysis. Not all samples are discussed further; those indicated in Table 1 with an  
180 asterisk were used in the calibration. The remaining samples imaged as part of the stack provides  
181 calibrated material for use in future work.

### 182 **Preparation for integrated 1, 2 and 3D measurement**

183 Olivine crystals were prepared by setting them in resin discs in order for them to cut, polished and  
184 analysed after the non-destructive XMT scans. This shape minimises the use of vertical field of  
185 view, and the flat upper and lower surfaces afford a stable platform on which to mount other  
186 material, which allows for ready insertion in later experiments (i.e. as internal standards). The  
187 diameter (14 mm) is suitable for re-use in laboratory XMT experiments in which  $<10\ \mu\text{m}$  pixel  
188 resolution is desirable.

189 Each disc was composed of a single layer of crystals, set in place using a two-part epoxy resin  
190 (Epothin<sup>®</sup>) using a soft plastic pipette tube as a mould (Fig. 1). The low initial viscosity of Epothin<sup>®</sup>  
191 wet olivine surfaces and limited the entrapment of air bubbles. The discs were then flattened with  
192 sandpaper to reduce the height of each to a minimum while still containing all the grains. Each disc  
193 was then labelled using an engraver (removal of resin means the label can be read in the X-ray  
194 images). A stack of the discs was made using double-sided tape, and was then mounted upon a  
195 resin pedestal made from the neck section of the pipette (Fig. 2).

196 Legacy olivine crystal mounts from Pankhurst et al. (2014) were cut down to  $\sim 1 \text{ cm}^2$ ,  $\sim 1 \text{ mm}$  thick  
197 chips using a combination of a Buehler PetroThin<sup>®</sup> thin-sectioning system, and a single edged razor  
198 blade. These pre-analysed crystals serve as secondary internal standards across a useful Fo range.  
199 The cores of these crystals are known to be homogenous from previous BSE imaging and EPMA  
200 data (Pankhurst et al., 2018a). The group of chips are labelled as one position in Fig. 1, see Table 1.

### 201 **X-ray micro-tomography imaging: monochromatic source**

202 To confirm that the relationship between linear attenuation and Fo-Fa solid solution is linear at a  
203 number of single energies, monochromatic X-ray beams were used. The olivine stack was imaged  
204 using 53, 60 and 70 kV beams at the Joint Engineering, Environmental and Processing (JEEP)  
205 beamline (i12; see Drakopoulos et al., 2015) at the Diamond Light Source Ltd., United Kingdom, to  
206 gather absorption image data at each single energy. These energies are typical of peak  
207 polychromatic beams used in laboratory X-ray sources to image igneous rocks up to a thickness of  
208  $\sim 2 \text{ cm}$  (e.g. Reyes-Dávila et al., 2016), which corresponds to the scale of a thin section. Camera  
209 module 2 was used which has a magnification of 0.82, a field of view of 20.3 mm in the horizontal  
210 and 15 mm usable in the vertical (per projection), with a pixel resolution of  $7.9 \mu\text{m}$ . A continuous  
211 helical scan-track (with a pitch of 10 mm) was used to collect projection data from the stack of  
212 samples in one scan. This allowed the entire sample to be imaged without increasing the  
213 horizontal field of view, which would have decreased resolution. In addition, this scan mode helps  
214 to significantly reduce ring artefacts within the reconstructed images (caused by the fixed  
215 defective regions on the detector). The raw projections were then pre-processed using the  
216 following techniques: (1) sinogram generation, which extracts tilted slices through the 3D helical  
217 datasets depending on the helical pitch; (2) zinger removal (Rivers, 1998), which removes artificial  
218 bright lines; (3) blob removal, which reduces the impact of dead region(s) on the detector; (4) ring  
219 removal, to clean up small ring artefacts that may remain (Vo et al., in prep); (5) center of rotation  
220 calculation (Vo et al., 2014). Finally, the volume was reconstructed by filtered back-projection  
221 (FBP; Ramachandran and Lakshminarayanan, 1971). All techniques are implemented in python  
222 codes (using h5py, scipy, numpy, pyfftw, and pyCUDA) by N. Vo.

### 223 **X-ray micro-tomography imaging: polychromatic sources**

224 The purpose of using a polychromatic beam from a non-synchrotron source was to provide a guide  
225 to the potential accuracy and precision of olivine chemical composition that can be achieved using  
226 an instrument common in many research environments. The stack was scanned using an FEI  
227 HeliScan system in Trondheim, Norway. Proprietary software was used to correct subtle beam  
228 hardening, which was largely avoided due to the high angle scanning approach. Data was supplied  
229 in 16-bit tiff format. Samples within the stack were also (circular) scanned at the Research  
230 Complex at Harwell using a Nikon 225 XTH system, using the polychromatic beam characterisation  
231 procedure described in Pankhurst et al. (2018b) to correct for beam hardening at specified density  
232 values (i.e. density of  $3.35 \text{ g/cm}^3$  for the disc containing shards of olivine from San Carlos).

### 233 **2D imaging and 1D chemical analysis**

234 Selected resin discs were prepared for electron probe microanalysis using standard materials (see  
235 Fig. 2 for analytical workflow). A JEOL electron probe micro-analyser (EPMA) 8320 Superprobe  
236 with five wavelength-dispersive (WD) spectrometers housed at the University of Leeds Electron  
237 Microscopy and Spectroscopy Centre was used to collect high resolution and high contrast  
238 backscattered electron (BSE) images. Brightness and contrast settings, which are normally  
239 adjusted according to user subjectivity and according to the feature of interest in each frame,  
240 were instead tuned to internal reference materials (San Carlos olivine: near detection limit; Fe-  
241 oxide; near saturation). EPMA spots (nominally 1  $\mu\text{m}$  size) were measured at the University of  
242 Iceland with the setup described in Pankhurst et al. (2017). While colour greater precision is able to  
243 be achieved using wider beams, higher current and longer analysis times, we wished to compare  
244 the XMT results with typical EPMA settings for olivine. Smithsonian Institution (Washington D.C.,  
245 USA) distributed micro-beam reference materials (RM) San Carlos Olivine (NMNH 111312-44) and  
246 Springwater Meteorite Olivine (USNM 2566) were used as primary and secondary RMs  
247 respectively.

248 The Springwater Meteorite RM returns precise major and minor oxide concentrations when run as  
249 a secondary standard (see Table 2). No significant drift was detected through the run, and as such  
250 we assign a maximum  $2\sigma$  uncertainty to each position of  $\pm 0.25$  mol % Fo.

251

## 252 **Building a calibration between techniques**

253 Positions of EPMA spot analyses were precisely located on BSE images in order to calibrate  
254 composition with BSE grayscale brightness, following the approach of Pankhurst (2018a). First, the  
255 BSE images were assessed using a variety of lookup tables in ImageJ (Rasband, 2015) to confirm  
256 homogeneity of the crystal cores or shards. Circles of 10  $\mu\text{m}$  diameter were located in regions of  
257 constant grayscale, which were then measured and deleted from the image to form a white  
258 'target'. Using the software CrossHair v1.1 (Lin, 2007), these spots could be co-located with high  
259 spatial accuracy using the JEOL interface, which also employs a crosshair location option. Two or  
260 three spot analyses were taken from the 10  $\mu\text{m}$  diameter position, in the core of each crystal or  
261 shard, and averaged. Thus, an appropriate level of spatial accuracy that links the chemical and  
262 image data was attained.

263 Optical microscope work and BSE images helped identify the locations of chemical spot analyses in  
264 the 3D images. These locations were checked for intensity gradients before values were recorded  
265 using ImageJ, using circular regions  $\sim 100$   $\mu\text{m}$  in diameter, recording the mean and standard  
266 deviation. We applied a non-local mean filter to the data for presentation purposes, but report all  
267 grayscale and  $2\sigma$  values after applying a 2-pixel median filter, which is well below the sampling  
268 resolution, yet necessary to minimise noise. It should be noted that it is possible to frame average  
269 using numerous projections at each angle. This would have the same effect (at least for the  
270 purpose here, since we do not ascribe meaning to features less than 5 pixels), yet would take  
271 almost an order of magnitude more instrument time to achieve the same image quality. The  
272 location reproducibility between 3D images is estimated at  $<10$   $\mu\text{m}$  in XY and  $<20$   $\mu\text{m}$  in Z, which is  
273 well below the voxel sampling resolution.

## 274 **Density calculations using X-ray attenuation**

275 Linear attenuation of olivine end-members at different X-ray energies were calculated using the  
276 National Institute of Standards and Technology Physical Measurement Laboratory Database;  
277 <https://physics.nist.gov/PhysRefData/Xcom/html/xcom1.html>. Results from this database are  
278 reported as mass attenuation coefficients, from which linear attenuation is derived simply as a



279 function of material density. Density values from Deer et al. (1982) were used and can be  
280 considered to scale as a linear function of composition (Bloss, 1952) across the range of interest  
281 here (Fo73-91). Thus attenuation is also predicted to be linear as a function of composition (Fig. 5).  
282 Values from online calculations are reported in the supplementary Table S1.

283 Calculations here assume a perfect solid solution between forsterite and fayalite, since tephroite  
284 (Tep; Mn end-member) is present only up to a few percent and has very similar density to fayalite.  
285 All other end members are in low enough abundance to warrant this assumption to a first order in  
286 typical igneous rocks (e.g. monticellite is rarely above half a percent). Values are expressed as Fo  
287 mol %, and implies the remainder is comprised of Fa and Tep.

288

## 289 **RESULTS**

290 Linear attenuation as measured by monochromatic X-rays, or image brightness values from  
291 polychromatic X-rays were extracted from tomograms and are presented in Table 3. The quality of  
292 the fayalite sample images was poor in comparison to the forsteritic samples; streak artefacts are  
293 evident (see Supplementary Figure 1). This is reflected in the considerable spread of linear  
294 attenuation values at constant chemical composition (Fo0).

295 Homogeneous brightness levels are observed in the cores of crystals in both polychromatic and  
296 backscatter electron image data (Fig. 3). The fayalite sample is the exception, this sample was too  
297 attenuating to be imaged satisfactorily (while using the same beam conditions as the rest of the  
298 stack). Relative image brightness (i.e. grayscale level) is in good qualitative agreement between  
299 the two (compare Fig. 3b i to iii and ii to iv).

300 Example calculations of linear attenuation according to solid solution chemistry are presented in  
301 the supplement, as are full EPMA results. Each tomographic image dataset is several gigabytes in  
302 size; we illustrate selected portions of these data as renders and slices in Figs 3 and 4, including  
303 comparisons to BSE images. Calibration of image data with chemical composition is illustrated in  
304 Figs. 5 and 6.

305

## 306 **DISCUSSION**

### 307 **Relationship between linear attenuation and composition**

308 Densitometric calculations predict that the olivine solid solution can be considered linear in the  
309 Fo73-91 range. Compositions measured by EPMA and linear attenuation ( $\mu$ ) are well correlated ( $R^2$   
310  $> 0.9$ ) at the three monochromatic energies (Fig. 5). It is likely that the particle size used for the  
311 fayalite (chosen to match the less dense, more forsteritic, samples) did not allow comparable  
312 transmission. This explains why, in addition to the wide spread of linear attenuation values, the  
313 average linear attenuation value for fayalite is slightly lower than that predicted from the Fo73-91  
314 array.

315 Discrepancy is also observed between calculated and measured  $\mu$  at any given position along the  
316 solid solution; the measured attenuation is lower than expected. This may be due to a scaling  
317 effect in detector response, although it is possible that the cause is associated with a property of  
318 the crystals themselves (i.e. leading to higher transmission than anticipated). While the measured  
319 and calculated trends do not match, their relative positions as a function of kV is the same.  
320 Whether this offset is a function of the imaging setup or reflective of a physical property of olivine,

321 neither poses a barrier for the practical application developed below. Current work is being  
322 undertaken to resolve why this offset occurs.

### 323 **An advance in measuring chemistry using quantitative densitometry**

324 Retrieving quantitative and reproducible image data of materials using polychromatic X-ray micro-  
325 computed tomography systems is an active field of research. The original technique was designed  
326 to provide qualitative information in medical and materials research in 3D, and thus instrument  
327 drift, optical and digital artefacts and scintillator degradation did not inhibit the collection of  
328 meaningful data. In contrast, these issues must be mitigated against to achieve useful,  
329 reproducible, quantitative image data.

330 Davis et al. (2015) showed that by first characterising a polychromatic beam using a step wedge,  
331 and then using a virtual phantom of the material of interest, a beam hardening correction could be  
332 derived. Then, the quantitative density distribution of simple materials could be calculated in 3D.  
333 While those authors' motivation was partly to map the mineral density of teeth, the approach is  
334 the same as ours. Rather than air 'diluting' the electron density of a single substance via a texture,  
335 we are measuring the relative proportions of end-member composition along a single solid  
336 solution, with a unique chemical result for a given density.

337 Helical scan data returns a linear fit to Fo content of crystal cores (Fig. 6a), and is shown to return  
338 higher precision (derived simply from image noise) than the synchrotron data. We reiterate that  
339 our intention was not to compare precision between monochromatic and polychromatic beams;  
340 increasing the length of each scan would result in higher signal:noise. The important result is that  
341 laboratory systems are shown produce at least the same quantitative measurement for olivine  
342 crystal cores in <1 hour than can be achieved with a synchrotron source in <10 min at 53 kV. The  
343 comparison is shown simply to demonstrate that laboratory source systems offer a practical and  
344 accessible solution to the construction of very large, quantitative, olivine crystal core datasets that  
345 have acceptable precision and accuracy with which to compare populations of crystals. Laboratory  
346 scans can be externally calibration using the procedures of Pankhurst et al. (2018b) and/or by  
347 using internal olivine standards.

348 In this study we have proven that within analytical uncertainty, the olivine solid solution has a  
349 linear response to both X-ray energy and Fo content in the range Fo<sub>73-91</sub>. The degree of variation in  
350 attenuation evident at the same composition may be due to crystallographic effects, although  
351 more study is required to resolve this question. This means that 3D chemical relationships  
352 between individual grains can be recovered using the attenuation of monochromatic and  
353 polychromatic X-ray beams.

### 354 **Present advantages and limitations**

355 A practical advantage of laboratory systems is that image resolution is scales with the field of view  
356 due to the conical beam shape. Reducing the distance between the sample and source improves  
357 the resolution. With a smooth 'zoom', the resolution can be optimised to the scale of interest. At  
358 synchrotron facilities that use a parallel beam, image resolution is essentially fixed by the camera  
359 module at any sample distance. Finally, the rapid developments in laboratory-source X-ray imaging  
360 systems, in particular improvements in electron gun stability, offer greatly enhanced  
361 reproducibility than earlier generations. Like any comparative technique, the use of internal  
362 standards is essential for calculating uncertainty, regardless of whether synchrotron or laboratory  
363 sources are used. Unlike EPMA, however, the standards and samples can be measured  
364 simultaneously (i.e. in the same field of view), which bypasses drift correction.

365 At crystal margins, where chemical zonation is both common and shown to contain valuable  
366 temporal information (e.g. Hartley et al., 2016; Pankhurst et al., 2018a), the comparison between  
367 BSE and laboratory X-ray images is encouraging, yet not sufficient at the resolution in the present  
368 study to retrieve quantitative data within  $\sim 100 \mu\text{m}$  from the crystal rim with comparable accuracy  
369 to EPMA (see Fig. 3). This is likely due to subtle beam hardening effects which are non-linear in  
370 regard to material composition, and also depend upon the region of interest's position in the  
371 sample itself. Method development to overcome these final limitations for application, for  
372 example, element diffusion modelling, is currently being researched. Optimisation techniques  
373 could combine 1) pre-filtering a polychromatic beam while retaining useful image contrast, 2) use  
374 of analogue phantoms of homogeneous composition that bracket that of the sample density in  
375 conjunction with 3) collecting beam intensity data (Pankhurst et al. 2018b) which would allow a  
376 researcher to tune beam-hardening correction factors *a posteriori* using (2) as monitors of beam  
377 hardening effects.

### 378 **San Carlos Olivine compositional variation**

379 The potential for some compositional mismatch between our olivine from San Carlos to that of the  
380 San Carlos SRM was anticipated from inter-laboratory comparisons using Smithsonian and non-  
381 Smithsonian material (Fournelle, 2011). Nevertheless, our results were unexpected. Despite  
382 originating from a single crystal, two distinct compositions were observed in the XMT data (Fig. 7).  
383 Each shards' grouping is corroborated by the BSE, EPMA and laboratory XMT data. Most shards  
384 are composed of Fo<sub>90.9</sub>, yet four pieces are slightly more evolved; all returning Fo<sub>89.1</sub>. This  
385 demonstrates that extremely subtle differences in olivine chemistry can be resolved by XMT

386 Each shard appeared to be homogeneous in BSE intensity across each shard is either flat or  
387 contains gradients corresponding to Fo variation far less than our EPMA uncertainty. These subtle  
388 gradients could be due to real variation, or a function of preparation. There is no relationship with  
389 Z distance (determined using the autofocus feature of the probe for EPMA software; Donovan et  
390 al., 2012), and the subtle tilt of the polished surface is unlikely to explain such gradients. It is  
391 conceivable that BSE signal intensity could be mediated by crystal orientation, yet if this was the  
392 case, and in a population of 11 randomly oriented shards, we should expect a spread of values  
393 rather than two distinct groups. Differences in polishing or perhaps even stage position (which  
394 might indicate an electrical bias in the chamber) can also be ruled out; the groupings are not  
395 spatially related. EPMA profiling including trace element mapping, and determination of  
396 crystallographic orientation, is planned for these shards, which may resolve these questions. The  
397 simplest explanation is that this single large crystal is zoned and comprised of distinct domains  
398 with relatively sharp boundaries between them. Further XMT work is planned for complete  
399 crystals.

400 Fournelle (2011) reported values across a range between  $\sim \text{Fo}_{88}$  to  $\text{Fo}_{91.5}$  for non-USNM San Carlos  
401 olivine, with the highest peak at  $\text{Fo}_{90.9}$  (Fig. 7). This composition corresponds to the group with the  
402 largest number of shards (group 2), and is consistent with a homogeneous core that dominates  
403 the volume of a crystal. The sub-dominant group 1 could be explained as being derived from a  
404 slightly more evolved overgrowth or diffusion rim, which is almost ubiquitous in volcanic olivine  
405 (e.g. Hartley et al., 2016; Kahl et al., 2011). The accepted value of USNM San Carlos Olivine is  
406 based on what is a comparatively tiny volume of crushed material which, intriguingly, sits between  
407 the two "extremes" (Fournelle, 2011).

### 408 **Investigating 3D chemistry and texture without a linking step**

409 Reconciling textural information with chemical data continues to drive petrologic research, and is  
410 an essential feature in any viable petrogenetic model. When measuring in 2D, however, there is

411 always some potential for chemical data to be mis-located in terms of its textural context. For  
412 example, the middle of a crystal in 2D is not necessarily its core. A measurement 100  $\mu\text{m}$  from a  
413 crystal rim in 2D could be less in 3D. Thus 2D measurements of texture and chemistry provide the  
414 potential to integrate information at a population level only (e.g. Morgan and Jerram, 2006). This  
415 is because what is measured from individual grains cannot be directly carried over to the third  
416 dimension due to these sectioning effects at the single-grain scale. Good representation is usually  
417 achieved simply by measuring over a wide enough area to capture a statistically meaningful  
418 dataset, yet these statistics do not provide context at the scale of individual grains. To link two-  
419 dimensional mineralogical observations to dynamic, physical processes that occur in three  
420 dimensions either some form of careful stereoscopic correction, extrapolation or reasoned  
421 assumption in regard to the third direction must be made (e.g. Morgan and Jerram, 2006). Current  
422 work is investigating olivine chemistry and size in natural rocks that contain other minerals.

423 In comparatively simple cases this does not preclude robust conclusions to be formed. However,  
424 since crystals can have complex histories (Kahl et al., 2013), population trends may not accurately  
425 reflect bulk magma behaviour or history. Technology that *inherently* links direct textural and  
426 chemical measurements overcomes the issue, since integration can be conducted at the grain  
427 scale. To aid definition of grain boundaries in samples that contain phases with similar attenuation  
428 to that of olivine, multiple X-ray tomographic techniques such as phase contrast imaging (Wang et  
429 al., in press; Wang et al., 2016a, b) can be used. Crystallographic orientation can also be  
430 determined using XMT (McDonald et al., 2015), which raises the possibility of extracting 3D maps  
431 of Fo content that are fully integrated with diffusion anisotropy for individual crystallographic  
432 domains.

433 Since these data are quantitative and reproducible, they are poised to address questions requiring  
434 fully integrated spatial and chemical context in 3D, and in in-situ experiments: 3D plus time (see  
435 Alvarez-Murga et al., 2017; Baker et al., 2012; Cai et al., 2014; Pistone et al., 2015).  
436 Monochromatic X-ray beams  $\leq 53$  kV are recommended to measure variation within single crystals  
437 to achieve enhanced contrasts (reducing uncertainty further) and to avoid beam hardening effects  
438 (compare the 53 with the 70 kV data in Fig. 5). The use of dual-energy laboratory X-ray systems  
439 (Liu et al., 2009) in geological research will likely allow quantitative 3D chemical measurement of  
440 mineral systems with three dominant end-members, such as pyroxene and feldspar.

441 XMT provides useful spatial context for the characterisation of new, and possibly existing, natural  
442 micro-beam standards. Such material must be homogeneous by definition. XMT provides a rapid  
443 method to determine how suitable a material might be, before comparatively more laborious  
444 analysis is conducted.

445 Quantitative X-ray micro-tomography can now provide raw data to further improve diffusion  
446 models (see Shea et al., 2015), targeting for in-situ Fe-Mg isotope analysis (Sio et al., 2013), and  
447 place such observations within full 3D textural analysis of olivine, which itself contains vital  
448 evidence for petrogenetic processes (Erdmann et al., 2014; Vinet and Higgins, 2011). With  
449 measurements of the volume, density and shape of crystals, physical behaviour (such as settling  
450 velocity) can be explored, and related back to chemical records in those crystals. Linking these  
451 insights will underpin developments such as determining dynamic processes in sills (e.g. Egorova  
452 and Latypov, 2013; Gibb and Henderson, 1992; Holness et al., 2017) crystal mushes (e.g. Thomson  
453 and Maclennan, 2013), and piecing together volcanic plumbing system behaviour (Pankhurst et al.,  
454 2018a).

455 Where a significant mass (10s to 100s mg) of olivine grains are required for isotopic  
456 measurements, checking an entire population of grains before chemical digestion can be difficult.  
457 Peridotite xenoliths, while not necessarily preserving direct evidence for melt-rock interaction in

458 the form of, for example, pyroxenite veins, may still preserve cryptic metasomatic effects of this  
459 process distal from the location of the pyroxenite itself. Screening olivine grains in crushed  
460 peridotite for chemical zoning derived from melt-rock interaction prior to digestion would be one  
461 such use of this technique. Another is obtaining 3D chemical information of olivine in-situ,  
462 providing context of such processes involved in the deposition, removal, and modification of  
463 accessory phases (Harvey et al., 2015).

464 There are a number of emergent “non-traditional” stable isotope systems where, as mass  
465 spectrometer sensitivity continues to improve, the transition from bulk-rock to mineral aggregate  
466 measurements, and toward single-grain and sub-grain measurement (Sio et al., 2013) will  
467 inevitably progress. Olivine is already of particular interest for Mg isotope studies (Chaussidon et  
468 al., 2017), and bulk-rock isotopic measurements of Fe (e.g. Huang et al., 2011), Ni (e.g. Gall et al.,  
469 2017) and Cr (e.g. Farkaš et al., 2013) are the vanguard for similar measurements on olivine  
470 aggregates. The proliferation of mass spectrometer amplifiers that can precisely record beam  
471 intensities of a few millivolts will mean that olivine mineral separates, demonstrably free of  
472 metasomatic effects prior to chemical preparation, will be critical for these applications.

## 473 **IMPLICATIONS AND APPLICATIONS OF 3D CHEMICAL MEASUREMENT OF OLIVINE**

474 Calibrated 3D X-ray images now can contain spatial and chemical information per voxel. A number  
475 of key advances are now possible:

- 476 • Crystal chemical populations can be fully integrated with size distributions, textural  
477 features and spatial relationships. These data will help unravel complex petrogenetic  
478 relationships in particular.
- 479 • Samples of extreme value can be chemically analysed using a non-destructive method.
- 480 • Composition can be tracked in 3D-plus-time during in-situ experiments.
- 481 • 3D olivine growth, dissolution and diffusion models can be tested using natural 3D data.
- 482 • Olivine separates can be screened for metasomatic effects prior to digestion and isotopic  
483 analysis.
- 484 • Microbeam standards can be screened for major element heterogeneity (entire existing  
485 mounts or material prior to mounting), and potentially reduce analytical inaccuracy due to  
486 standard inhomogeneity.

## 487 **ACKNOWLEDGEMENTS**

488 This work was conducted under the auspices of an AXA Research Fund Fellowship to MJP and  
489 NERC grant (UK) grant NE/M013561/1. Synchrotron tomography was undertaken on I12 at  
490 Diamond Light Source under proposals EE14033-1 and EE14033-2. The British Natural History  
491 Museum, Thor Thordarson, Godfrey Fitton, Michael Turner and Iain Smith are gratefully  
492 acknowledged for providing samples of olivine and/or olivine-rich naturally occurring rocks. Tom  
493 Shea and Tomoaki Morishita are thanked for their thoughtful and thorough reviews which  
494 improved the manuscript. Julia Hammer is thanked for her editorial handling.

495

## 496 **DATA STATEMENT**

497 Representative samples of the research data are shown in the figures. Other datasets generated  
498 during and/or analysed during this study are not publicly available due to their large size but are  
499 available from the corresponding author on reasonable request.

500

501 **REFERENCES**

- 502 Alvarez-Murga, M., Perrillat, J. P., Le Godec, Y., Bergame, F., Philippe, J., King, A., Guignot, N., Mezouar, M.,  
503 and Hodeau, J. L., 2017, Development of synchrotron X-ray micro-tomography under extreme  
504 conditions of pressure and temperature: *Journal of Synchrotron Radiation*, v. 24, no. 1, p. 240-247.
- 505 Anderson, P., Levinkind, M., and Elliott, J. C., 1998, Scanning microradiographic studies of rates of in vitro  
506 demineralization in human and bovine dental enamel: *Archives of Oral Biology*, v. 43, no. 8, p. 649-  
507 656.
- 508 Baker, D. R., Brun, F., O'Shaughnessy, C., Mancini, L., Fife, J. L., and Rivers, M., 2012, A four-dimensional X-  
509 ray tomographic microscopy study of bubble growth in basaltic foam: *Nature Communications*, v. 3,  
510 p. 1135.
- 511 Berger, M. J., Hubbell, J., Seltzer, S., Chang, J., Coursey, J., Sukumar, R., Zucker, D., and Olsen, K., 2016,  
512 XCOM: Photon cross sections database, NIST Standard reference database, Volume 8, p. 3587-  
513 3597.
- 514 Bloss, F., 1952, Relationship between density and composition in mol per-cent for some solid solution  
515 series: *American Mineralogist*, v. 37, no. 11-1, p. 966-981.
- 516 Bryon, D., Atherton, M., and Hunter, R., 1995, The interpretation of granitic textures from serial thin  
517 sectioning, image analysis and three-dimensional reconstruction: *Mineralogical Magazine*, v. 59, no.  
518 2, p. 203-211.
- 519 Cai, B., Karagadde, S., Yuan, L., Marrow, T. J., Connolley, T., and Lee, P. D., 2014, In situ synchrotron  
520 tomographic quantification of granular and intragranular deformation during semi-solid  
521 compression of an equiaxed dendritic Al-Cu alloy: *Acta Materialia*, v. 76, p. 371-380.
- 522 Chaussidon, M., Deng, Z., Villeneuve, J., Moureau, J., Watson, B., Richter, F., and Moynier, F., 2017, In Situ  
523 Analysis of Non-Traditional Isotopes by SIMS and LA-MC-ICP-MS: Key Aspects and the Example of  
524 Mg Isotopes in Olivines and Silicate Glasses: *Reviews in Mineralogy and Geochemistry*, v. 82, no. 1,  
525 p. 127-163.
- 526 Cnudde, V., and Boone, M. N., 2013, High-resolution X-ray computed tomography in geosciences: A review  
527 of the current technology and applications: *Earth-Science Reviews*, v. 123, no. 0, p. 1-17.
- 528 Cooper, M. R., and Hunter, R. H., 1995, Precision serial lapping, imaging and threedimensional  
529 reconstruction of minus-cement and post-cementation intergranular pore-systems in the Penrith  
530 Sandstone of north-western England: *Mineralogical Magazine*, v. 59, no. 2, p. 213-220.
- 531 Davis, G. R., Evershed, A. N. Z., and Mills, D., 2015, Characterisation of materials: determining density using  
532 X-ray microtomography: *Materials and Science and Technology*, v. 31, no. 2, p. 162-166.
- 533 Deer, W., Howie, R. A., and Zussman, J., 1982, *Rock-forming minerals*. vol. 1 A; orthosilicates, Longman, UK,  
534 919p.
- 535 Deer, W. A., Howie, R. A., and Zussman, J., 1992, *An introduction to the rock-forming minerals*, Longman  
536 London.
- 537 Denison, C., and Carlson, W. D., 1997, Three-dimensional quantitative textural analysis of metamorphic  
538 rocks using high-resolution computed X-ray tomography: Part II. Application to natural samples:  
539 *Journal of Metamorphic Geology*, v. 15, no. 1, p. 45-57.
- 540 Donovan, J., Kremser, D., and Fournelle, J., 2012, Probe for EPMA: acquisition, automation and analysis:  
541 Probe Software, Inc., Eugene, Oregon.
- 542 Drakopoulos, M., Connolley, T., Reinhard, C., Atwood, R., Magdysyuk, O., Vo, N., Hart, M., Connor, L.,  
543 Humphreys, B., and Howell, G., 2015, I12: The joint engineering, environment and processing (JEEP)  
544 beamline at diamond light source: *Journal of Synchrotron Radiation*, v. 22, no. 3, p. 828-838.
- 545 Egorova, V., and Latypov, R., 2013, Mafic-Ultramafic Sills: New Insights from M- and S-shaped Mineral and  
546 Whole-rock Compositional Profiles: *Journal of Petrology*, v. 54, no. 10, p. 2155-2191.
- 547 Erdmann, S., Scaillet, B., Martel, C., and Cadoux, A., 2014, Characteristic Textures of Recrystallized,  
548 Peritectic, and Primary Magmatic Olivine in Experimental Samples and Natural Volcanic Rocks:  
549 *Journal of Petrology*, v. 55, no. 12, p. 2377-2402.
- 550 Farkaš, J., Chrástný, V., Novák, M., Čadkova, E., Pašava, J., Chakrabarti, R., Jacobsen, S. B., Ackerman, L., and  
551 Bullen, T. D., 2013, Chromium isotope variations ( $\delta^{53/52}\text{Cr}$ ) in mantle-derived sources and their  
552 weathering products: Implications for environmental studies and the evolution of  $\delta^{53/52}\text{Cr}$  in the  
553 Earth's mantle over geologic time: *Geochimica et Cosmochimica Acta*, v. 123, p. 74-92.

554 Flannery, B. P., Deckman, H. W., Roberge, W. G., and D'Amico, K. L., 1987, Three-Dimensional X-Ray  
555 Microtomography: *Science*, v. 237, no. 4821, p. 1439-1444.

556 Fonseca, J., O'Sullivan, C., Coop, M. R., and Lee, P. D., 2013, Quantifying the evolution of soil fabric during  
557 shearing using directional parameters: *Geotechnique*, v. 63, no. 6, p. 487-499.

558 Fournelle, J., 2011, An Investigation of "San Carlos Olivine": Comparing USNM-distributed Material with  
559 Commercially Available Material: *Microscopy and Microanalysis*, v. 17, no. SupplementS2, p. 842-  
560 843.

561 Gall, L., Williams, H. M., Halliday, A. N., and Kerr, A. C., 2017, Nickel isotopic composition of the mantle:  
562 *Geochimica et Cosmochimica Acta*, v. 199, p. 196-209.

563 Gibb, F. G. F., and Henderson, c. M. B., 1992, Convection and crystal settling in sills: Contributions to  
564 *Mineralogy and Petrology*, v. 109, no. 4, p. 538-545.

565 Hall, S., Bornert, M., Desrues, J., Pannier, Y., Lenoir, N., Viggiani, G., and Bésuelle, P., 2010, Discrete and  
566 continuum analysis of localised deformation in sand using X-ray  $\mu$ CT and volumetric digital image  
567 correlation: *Géotechnique*, v. 60, no. 5, p. 315-322.

568 Hartley, M. E., Morgan, D. J., Maclennan, J., Edmonds, M., and Thordarson, T., 2016, Tracking timescales of  
569 short-term precursors to large basaltic fissure eruptions via Fe–Mg diffusion in olivine: *EPSL*, v. 439,  
570 p. 58-70.

571 Harvey, J., König, S., and Luguet, A., 2015, The effects of melt depletion and metasomatism on highly  
572 siderophile and strongly chalcophile elements: S-Se-Te-Re-PGE systematics of peridotite xenoliths  
573 from Kilbourne Hole, New Mexico: *Geochimica et Cosmochimica Acta*, v. 166, p. 210-233.

574 Harvey, J., Yoshikawa, M., Hammond, S. J., and Burton, K. W., 2012, Deciphering the trace element  
575 characteristics in Kilbourne Hole peridotite xenoliths: melt–rock interaction and metasomatism  
576 beneath the Rio Grande Rift, SW USA: *Journal of Petrology*, v. 53, no. 8, p. 1709-1742.

577 Holness, M. B., Farr, R., and Neufeld, J. A., 2017, Crystal settling and convection in the Shiant Isles Main Sill:  
578 *Contributions to Mineralogy and Petrology*, v. 172, no. 1, p. 7.

579 Holtzman, B., Kohlstedt, D., Zimmerman, M., Heidelbach, F., Hiraga, T., and Hustoft, J., 2003, Melt  
580 segregation and strain partitioning: implications for seismic anisotropy and mantle flow: *Science*, v.  
581 301, no. 5637, p. 1227-1230.

582 Huang, F., Zhang, Z., Lundstrom, C. C., and Zhi, X., 2011, Iron and magnesium isotopic compositions of  
583 peridotite xenoliths from Eastern China: *Geochimica et Cosmochimica Acta*, v. 75, no. 12, p. 3318-  
584 3334.

585 Jahanbagloo, I., 1969, X-ray diffraction study of olivine solid solution series: *American Mineralogist*, v. 54,  
586 no. 1-2, p. 246-+.

587 Jarosewich, E., Nelen, J. A., and Norberg, J. A., 1980, Reference Samples for Electron Microprobe Analysis:  
588 *Geostandards Newsletter*, v. 4, no. 1, p. 43-47.

589 Jerram, D. A., Dobson, K. J., Morgan, D. J., and Pankhurst, M. J., 2018, The Petrogenesis of Magmatic  
590 Systems: Using Igneous Textures to Understand Magmatic Processes, *in* Burchardt, S., ed., *Volcanic  
591 and Igneous Plumbing Systems*, Elsevier, p. 191-229.

592 Jerram, D. A., Mock, A., Davis, G. R., Field, M., and Brown, R. J., 2009, 3D crystal size distributions: A case  
593 study on quantifying olivine populations in kimberlites: *Lithos*, v. 112, Supplement 1, no. 0, p. 223-  
594 235.

595 Kahl, M., Chakraborty, S., Costa, F., and Pompilio, M., 2011, Dynamic plumbing system beneath volcanoes  
596 revealed by kinetic modeling, and the connection to monitoring data: An example from Mt. Etna:  
597 *Earth and Planetary Science Letters*, v. 308, no. 1-2, p. 11-22.

598 Kahl, M., Chakraborty, S., Costa, F., Pompilio, M., Liuzzo, M., and Viccaro, M., 2013, Compositionally zoned  
599 crystals and real-time degassing data reveal changes in magma transfer dynamics during the 2006  
600 summit eruptive episodes of Mt. Etna: *Bulletin of Volcanology*, v. 75, no. 2, p. 1-14.

601 Ketcham, R. A., 2005, Computational methods for quantitative analysis of three-dimensional features in  
602 geological specimens: *Geosphere*, v. 1, no. 1, p. 32-41.

603 Ketcham, R. A., and Carlson, W. D., 2001, Acquisition, optimization and interpretation of X-ray computed  
604 tomographic imagery: applications to the geosciences: *Computers & Geosciences*, v. 27, no. 4, p.  
605 381-400.

606 Kile, D. E., 2009, The universal stage: The past, present, and future of a mineralogical research instrument:  
607 *Geochemical News*, v. 140, no. 8.

608 Leber, A. W., Knez, A., Becker, A., Becker, C., von Ziegler, F., Nikolaou, K., Rist, C., Reiser, M., White, C.,  
609 Steinbeck, G., and Boekstegers, P., 2004, Accuracy of multidetector spiral computed tomography in  
610 identifying and differentiating the composition of coronary atherosclerotic plaques. A comparative  
611 study with intracoronary ultrasound.: *Journal of the American College of Cardiology*, v. 43, no. 7, p.  
612 1241-1247.

613 Lemelle, L., Simionovici, A., Truche, R., Rau, C., Chukalina, M., and Gillet, P., 2004, A new nondestructive X-  
614 ray method for the determination of the 3D mineralogy at the micrometer scale: *American*  
615 *Mineralogist*, v. 89, no. 4, p. 547-553.

616 Lin, M., 2007, CrossHair v1.1.

617 Lin, Q., Neethling, S., Courtois, L., Dobson, K., and Lee, P., 2016, Multi-scale quantification of leaching  
618 performance using X-ray tomography: *Hydrometallurgy*, v. 164, p. 265-277.

619 Liu, X., Yu, L., Primak, A. N., and McCollough, C. H., 2009, Quantitative imaging of element composition and  
620 mass fraction using dual-energy CT: Three-material decomposition: *Medical Physics*, v. 36, no. 5, p.  
621 1602-1609.

622 Ma, L., Taylor, K. G., Lee, P. D., Dobson, K. J., Dowe, P. J., and Courtois, L., 2016, Novel 3D centimetre-to  
623 nano-scale quantification of an organic-rich mudstone: The Carboniferous Bowland Shale, Northern  
624 England: *Marine and Petroleum Geology*, v. 72, p. 193-205.

625 Macente, A., Fusses, F., Menegon, L., Xianghui, X., and John, T., 2017, The strain-dependent spatial  
626 evolution of garnet in a high-pressure ductile shear zone from the Western Gneiss Region  
627 (Norway): a synchrotron X-ray microtomography study: *Journal of Metamorphic Geology*.

628 Marteau, J., Gibert, D., Lesparre, N., Nicollin, F., Noli, P., and Giacoppo, F., 2012, Muons tomography  
629 applied to geosciences and volcanology: *Nuclear Instruments and Methods in Physics Research*  
630 *Section A: Accelerators, Spectrometers, Detectors and Associated Equipment*, v. 695, no.  
631 Supplement C, p. 23-28.

632 McDonald, S., Reischig, P., Holzner, C., Lauridsen, E., Withers, P., Merkle, A., and Feser, M., 2015, Non-  
633 destructive mapping of grain orientations in 3D by laboratory X-ray microscopy: *Scientific Reports*,  
634 v. 5.

635 Mizukami, T., Wallis, S. R., and Yamamoto, J., 2004, Natural examples of olivine lattice preferred orientation  
636 patterns with a flow-normal a-axis maximum: *Nature*, v. 427, no. 6973, p. 432.

637 Mock, A., and Jerram, D. A., 2005, Crystal Size Distributions (CSD) in Three Dimensions: Insights from the 3D  
638 Reconstruction of a Highly Porphyritic Rhyolite: *Journal of Petrology*, v. 46, no. 8, p. 1525-1541.

639 Morgan, D. J., and Jerram, D. A., 2006, On estimating crystal shape for crystal size distribution analysis:  
640 *Journal of Volcanology and Geothermal Research*, v. 154, no. 1-2, p. 1-7.

641 Nakashima, Y., 2000, The use of X-ray CT to measure diffusion coefficients of heavy ions in water-saturated  
642 porous media: *Engineering Geology*, v. 56, no. 1, p. 11-17.

643 Pankhurst, M. J., Dobson, K. J., Morgan, D. J., Loughlin, S. C., Thordarson, T., Courtios, L., and Lee, P. D.,  
644 2014, Directly monitoring the magmas fuelling volcanic eruptions in near-real-time using X-ray  
645 micro-computed tomography: *Journal of Petrology*, v. 55, no. 3, p. 671-684.

646 Pankhurst, M. J., Morgan, D. J., Thordarson, T., and Loughlin, S. C., 2018a, Magmatic crystal records in time,  
647 space, and process, causatively linked with volcanic unrest: *Earth and Planetary Science Letters*, v.  
648 493, p. 231-241.

649 Pankhurst, M. J., Fowler, R., Courtois, L., Nonni, S., Zuddas, F., Atwood, R. C., Davis, G. R., and Lee, P. D.,  
650 2018b, Enabling three-dimensional densitometric measurements using laboratory source X-ray  
651 micro-computed tomography: *SoftwareX*, v. 7, p. 115-121.

652 Pankhurst, M. J., Walshaw, R., and Morgan, D. J., 2017, Major Element Chemical Heterogeneity in Geo2  
653 Olivine Microbeam Reference Material: A Spatial Approach to Quantifying Heterogeneity in Primary  
654 Reference Materials: *Geostandards and Geoanalytical Research*, v. 41, no. 1, p. 85-91.

655 Philpotts, A. R., Brustman, C. M., Shi, J., Carlson, W. D., and Denison, C., 1999, Plagioclase-chain networks in  
656 slowly cooled basaltic magma: *American Mineralogist*, v. 84, no. 11-12, p. 1819-1829.

657 Pistone, M., Caricchi, L., Fife, J. L., Mader, K., and Ulmer, P., 2015, In situ X-ray tomographic microscopy  
658 observations of vesiculation of bubble-free and bubble-bearing magmas: *Bulletin of Volcanology*, v.  
659 77, no. 12, p. 108.

660 Poldervaart, A., 1950, Correlation of physical properties and chemical composition in the plagioclase,  
661 olivine, and orthopyroxene series: *American Mineralogist*, v. 35, no. 11-1, p. 1067-1079.



662 Ramachandran, G., and Lakshminarayanan, A., 1971, Three-dimensional reconstruction from radiographs  
663 and electron micrographs: application of convolutions instead of Fourier transforms: Proceedings  
664 of the National Academy of Sciences, v. 68, no. 9, p. 2236-2240.

665 Rasband, W. S., 2015, ImageJ: Bethesda, Maryland, USA, 1997-2015, US National Institutes of Health.

666 Reyes-Dávila, G. A., Arámbula-Mendoza, R., Espinasa-Pereña, R., Pankhurst, M. J., Navarro-Ochoa, C.,  
667 Savov, I., Vargas-Bracamontes, D. M., Cortés-Cortés, A., Gutiérrez-Martínez, C., Valdés-González, C.,  
668 Domínguez-Reyes, T., González-Amezcuca, M., Martínez-Fierros, A., Ramírez-Vázquez, C. A.,  
669 Cárdenas-González, L., Castañeda-Bastida, E., Vázquez Espinoza de los Monteros, D. M., Nieto-  
670 Torres, A., Campion, R., Courtois, L., and Lee, P. D., 2016, Volcán de Colima dome collapse of July,  
671 2015 and associated pyroclastic density currents: Journal of Volcanology and Geothermal Research,  
672 v. 320, p. 100-106.

673 Reyes, F., Lin, Q., Udoudo, O., Dodds, C., Lee, P., and Neethling, S., 2017, Calibrated X-ray micro-  
674 tomography for mineral ore quantification: Minerals Engineering, v. 110, p. 122-130.

675 Rivers, M., 1998, Tutorial introduction to X-ray computed microtomography data processing: University of  
676 Chicago.

677 Rudraswami, N., Prasad, M. S., Jones, R., and Nagashima, K., 2016, In situ oxygen isotope compositions in  
678 olivines of different types of cosmic spherules: An assessment of relationships to chondritic  
679 particles: Geochimica et Cosmochimica Acta, v. 194, p. 1-14.

680 Shea, T., Costa, F., Krimer, D., and Hammer, J. E., 2015, Accuracy of timescales retrieved from diffusion  
681 modeling in olivine: A 3D perspective: American Mineralogist, v. 100, p. 2026-2042.

682 Sigmundsson, F., Hreinsdóttir, S., Hooper, A., Árnadóttir, T., Pedersen, R., Roberts, M. J., Óskarsson, N.,  
683 Auriac, A., Decriem, J., Einarsson, P., Geirsson, H., Hensch, M., Ófeigsson, B. G., Sturkell, E.,  
684 Sveinbjörnsson, H., and Feigl, K. L., 2010, Intrusion triggering of the 2010 Eyjafjallajökull explosive  
685 eruption: Nature, v. 468, no. 7322, p. 426-432.

686 Sio, C. K. I., Dauphas, N., Teng, F.-Z., Chaussidon, M., Helz, R. T., and Roskosz, M., 2013, Discerning crystal  
687 growth from diffusion profiles in zoned olivine by in situ Mg-Fe isotopic analyses: Geochimica et  
688 Cosmochimica Acta, v. 123, p. 302-321.

689 Sorby, H. C., 1858, On the microscopical, structure of crystals, indicating the origin of minerals and rocks:  
690 Quarterly Journal of the Geological Society, v. 14, no. 1-2, p. 453-500.

691 Sparks, S. R. J., Sigurdsson, H., and Wilson, L., 1977, Magma mixing: a mechanism for triggering acid  
692 explosive eruptions: Nature, v. 267, no. 5609, p. 315-318.

693 Suuronen, J.-P., and Sayab, M., 2018, 3D nanopetrography and chemical imaging of datable zircons by  
694 synchrotron multimodal X-ray tomography: Scientific Reports, v. 8, no. 1, p. 4747.

695 Thomson, A., and Maclennan, J., 2013, The Distribution of Olivine Compositions in Icelandic Basalts and  
696 Picrites: Journal of Petrology, v. 54, no. 4, p. 745-768.

697 Vinet, N., and Higgins, M. D., 2011, What can crystal size distributions and olivine compositions tell us  
698 about magma solidification processes inside Kilauea Iki lava lake, Hawaii?: Journal of Volcanology  
699 and Geothermal Research, v. 208, no. 3-4, p. 136-162.

700 Vo, N. T., Drakopoulos, M., and Atwood, R. C., in prep, Superior techniques for eliminating ring artifacts in  
701 X-ray micro-tomography.

702 Vo, N. T., Drakopoulos, M., Atwood, R. C., and Reinhard, C., 2014, Reliable method for calculating the  
703 center of rotation in parallel-beam tomography: Optics express, v. 22, no. 16, p. 19078-19086.

704 Wang, H., Cai, B., Pankhurst, M. J., Zhou, T., Kashyap, Y., Atwood, R., Le Gall, N., Lee, P., Drakopoulos, M.,  
705 and Sawhney, K., in press, X-ray phase-contrast imaging with engineered porous materials over 50  
706 keV: Journal of Synchrotron Radiation.

707 Wang, H., Kashyap, Y., and Sawhney, K., 2016a, From synchrotron radiation to lab source: advanced  
708 speckle-based X-ray imaging using abrasive paper: Scientific reports, v. 6.

709 -, 2016b, Quantitative X-ray dark-field and phase tomography using single directional speckle scanning  
710 technique: Applied Physics Letters, v. 108, no. 12, p. 124102.

711 Whitney, D. L., and Evans, B. W., 2010, Abbreviations for names of rock-forming minerals: American  
712 Mineralogist, v. 95, no. 1, p. 185-187.

713 Winkler, B., Knorr, K., Kahle, A., Vontobel, P., Lehmann, E., Hennion, B., and Bayon, G., 2002, Neutron  
714 imaging and neutron tomography as non-destructive tools to study bulk-rock samples: European  
715 Journal of Mineralogy, v. 14, no. 2, p. 349-354.

716 Yue, S., Lee, P. D., Poologasundarampillai, G., and Jones, J. R., 2011, Evaluation of 3-D bioactive glass  
717 scaffolds dissolution in a perfusion flow system with X-ray microtomography: *Acta Biomaterialia*, v.  
718 7, no. 6, p. 2637-2643.  
719

720 **Tables**

721

722 *Table 1. Description, source, and position of olivine sample discs arranged in a stack and scanned in*  
 723 *XMT systems.*

Position of disc in stack (see Fig. 2)	Sample description	Source/reference
1	Legacy crystals cut from grain mounts	Pankhurst et al. (2014)
2*	+1 mm sized crystals from the 2010 flank eruption of Eyjafjallajökull (Fimmvörðuháls: F07a above b).	T. Thordarson
3	Killbourne Hole Peridotite olivine.	Harvey et al. (2012)
4	Háleyjarbunga lava shield (picrite) olivine.	G. Fitton/T. Thordarson
5	Star-1 (alkali basalt; Papua New Guinea).	M. Turner/I. Smith
6	Green Sand Beach (Hawaii).	G. Fitton
7*	San Carlos Forsterite.	J. Harvey
8	Rockport Fayalite.	Natural History Museum, London, UK (BM.1985, MI8988)
9	Eyjafjallajökull Summit eruption (2010, Iceland) E60: b above a.	T. Thordarson

*\*Indicates samples used for primary calibration here, the other samples were not analysed by EPMA (i.e. cut ground and polished). Instead, they were retained to be used as internal reference materials in subsequent work.*

724

725

726 *Table 2. Electron Probe Microanalysis secondary reference material results. Individual oxide results*  
 727 *are accurate within 2σ of accepted values. Note the precision on major oxides used to calculate Fo*  
 728 *content: FeO, MgO and MnO (Mn was included in all Fo calculations due to its comparatively high*  
 729 *abundance in the fayalite sample). The exception is SiO<sub>2</sub>, which is known to give inferior results in*  
 730 *the type specimen. Since the Mg and Fe content dominate the attenuation contrast in the solid*  
 731 *solution of interest here, no added uncertainty is ascribed to the data.*

Springwater Meteorite olivine			
Oxide	As secondary RM		Accepted value
	(n=44)		(Jarosewich et al., 1980)
	wt %	2σ	wt %
SiO <sub>2</sub>	39.76	0.31	38.95
TiO <sub>2</sub>	0.08	0.04	nr
Al <sub>2</sub> O <sub>3</sub>	bd	na	nr
Cr <sub>2</sub> O <sub>3</sub>	0.04	0.02	0.02
FeO	16.64	0.23	16.62
MnO	0.31	0.02	0.3
MgO	43.65	0.42	43.58
CaO	bd		nr
Total	100.21	0.74	99.47
Forsterite %*	82.38	±0.25	82.11

bd = below detection, na = not applicable, nr = not reported

\*calculated using Fe, Mg and Mn as per all EPMA calculations presented here

732

733

734 Table 3. Crystal core Fo content, calculated density, and image data.

Crystal core	Fo*	Density**		Polychromatic data		Monochromatic data	
		g/cm <sup>3</sup>	5% error	Intensity (16-bit)	2 $\sigma$	u (53 kV)	2 $\sigma$
ol3†	75.03	3.55	0.18	12819	61	1.43	0.09
ol4	76.29	3.54	0.18	12732	74	1.38	0.11
ol6	75.22	3.55	0.18	12816	69	1.44	0.11
ol7	78.18	3.52	0.18	12561	105		0.00
ol8	79.92	3.50	0.17	12571	82	1.29	0.09
ol9	79.75	3.50	0.17	12571	67	1.29	0.10
ol10	76.28	3.54	0.18	12789	70		0.00
ol11	78.37	3.51	0.18	12695	61	1.36	0.09
ol12	80.54	3.49	0.17	12491	62	1.30	0.09
ol13	80.73	3.49	0.17		84		0.00
ol15	79.86	3.50	0.17	12547	59	1.29	0.10
ol16	85.70	3.43	0.17	12139	172	1.13	0.11
ol17	78.45	3.51	0.18	12634	77	1.38	0.09
ol18	73.96	3.56	0.18		155	1.48	0.09
ol19	74.09	3.56	0.18	12768	67	1.45	0.12
ol20	74.03	3.56	0.18	12793	66	1.46	0.12
ol21	87.11	3.42	0.17	12172	65	1.13	0.09
ol22	81.53	3.48	0.17	12380	138	1.28	0.10
ol23	86.19	3.43	0.17	12196	72	1.16	0.08
ol24	77.58	3.52	0.18	12604	85	1.36	0.08
ol25	80.36	3.49	0.17	12504	65	1.32	0.12
ol26	80.50	3.49	0.17	12500	62	1.32	0.09
ol27	83.29	3.46	0.17		67		0.00
ol28	87.04	3.42	0.17	12144	60	1.13	0.09
ol29	78.53	3.51	0.18	12595	64	1.32	0.08

ol30	79.45	3.50	0.18	12532	71	1.34	0.12
ol31	78.08	3.52	0.18	12595	85	1.39	0.11
ol32	75.92	3.54	0.18	12745	56	1.41	0.08
ol33	73.57	3.57	0.18	12841	71	1.48	0.11
ol34	78.90	3.51	0.18	12517	88	1.32	0.10
ol35	80.10	3.49	0.17	12501	69	1.34	0.08
SC_1	90.95	3.37	0.17	11947	29	1.03	0.15
SC_2	90.92	3.37	0.17	11976	25	1.04	0.14
SC_3	90.92	3.37	0.17	11958	29	1.06	0.16
SC_4	89.10	3.39	0.17	12099	33	1.10	0.16
SC_5	90.89	3.37	0.17	11988	34	1.03	0.13
SC_6	89.08	3.39	0.17	12061	52	1.07	0.18
SC_7	90.96	3.37	0.17	11978	59	0.97	0.16
SC_9	90.93	3.37	0.17	11970	32	1.04	0.15
SC_10	89.09	3.39	0.17	12057	33	1.08	0.14
SC_11	90.87	3.37	0.17	11951	34	1.03	0.14
*average values per crystal core (see Table S2 for full results)							
**calculated from numerical mixing of Fo and Fa end-members							
†olXX are abbreviated from FMVD7_1mm_a_olXX (see Table S2)							

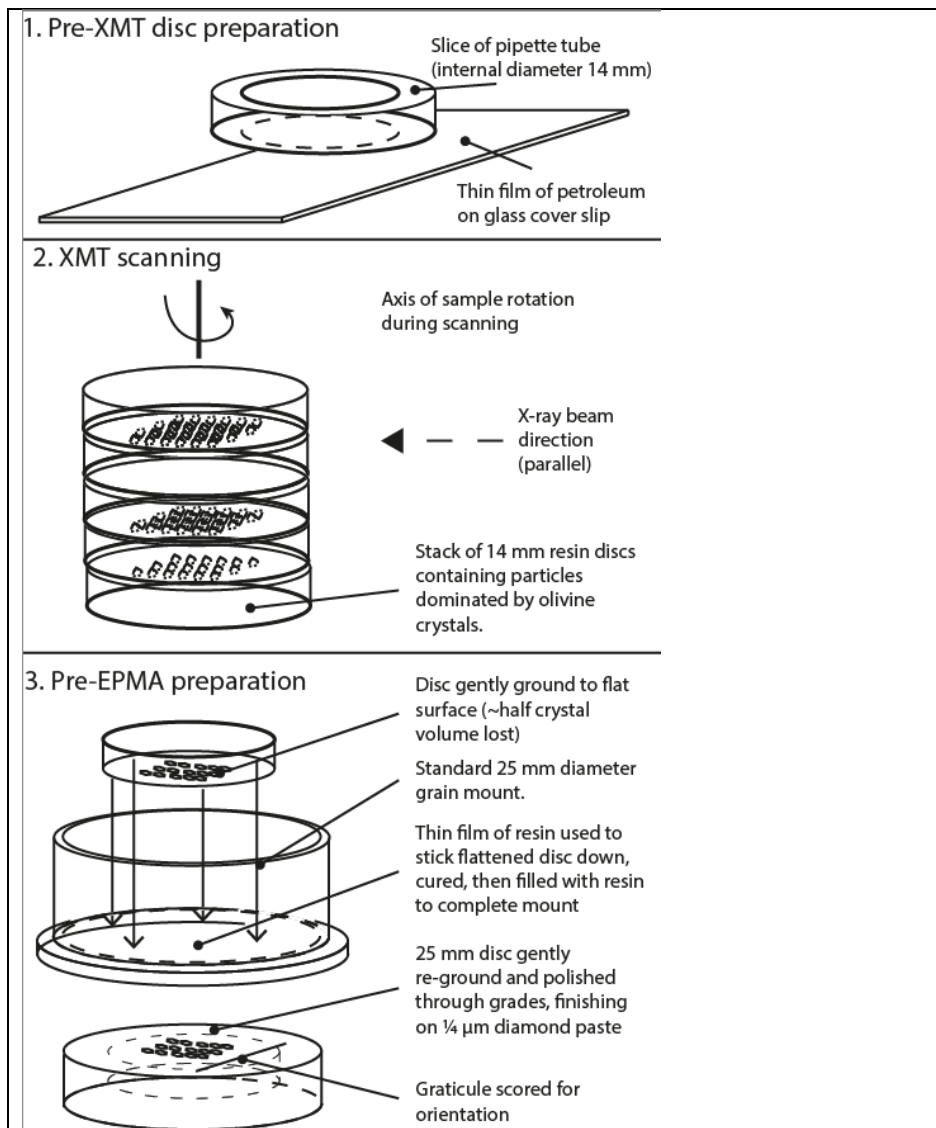


**Fig. 1. Schematic of sample preparation for integrated XMT and 2D analysis.** 1) Crystals were first set into 14 mm diameter resin discs, 2) scanned, and 3) selected discs were prepared into standard 25 mm mounts for a variety of 2D analysis.

745

746

747

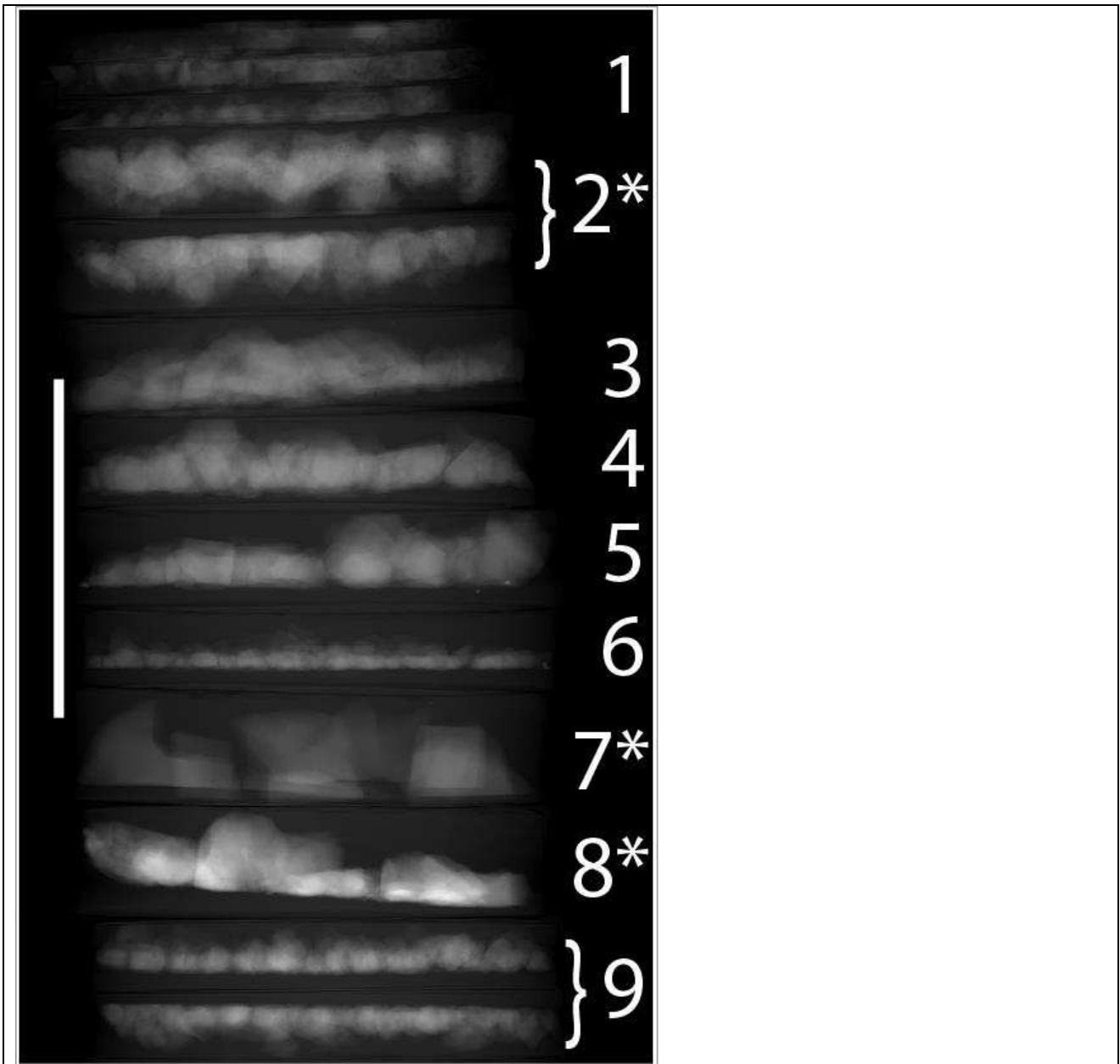


Fig. 2. **Re-projection image from reconstruction of stack.** Stack is comprised of resin discs that each contain a sample (or sample subset) of olivine. Refer to Table 1 for sample descriptions. White bar is 10 mm. \*Indicates samples investigated with BSE imaging and EPMA.

748

749



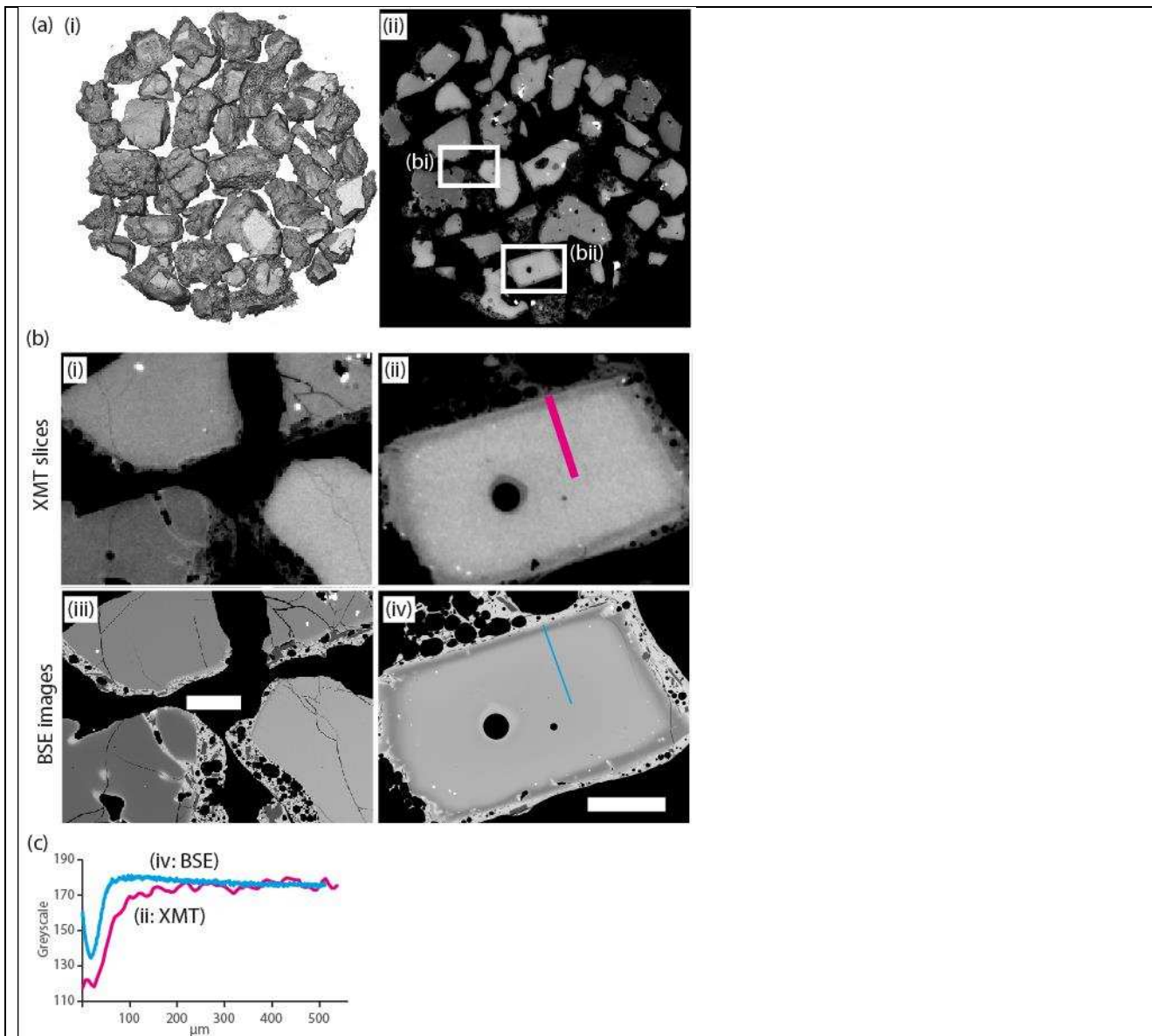


Fig. 3. Illustration of comparative 3D and 2D imaging techniques focussed upon the mineral olivine. In most cases these particles retained some vesiculated glassy matrix around the olivine crystals after being hand-picked from loose tephra. a) 3D image data from polychromatic beam, field of view = 8 mm. i) volume render of Fimmvörðuháls sample (sample 2a in stack) ii) XY orthoslice through attenuation image; insets correspond to b). b) Comparison between XMT slices (i and ii) and BSE images (iii and iv), white bars = 0.5 mm, no image filtering was performed. c) image intensity profiles from the same location in XMT and BSE data. Each line is 10 pixels wide. A qualitative match is observed: a reverse zone (darker – more Mg rich) is observed around a homogeneous core. The shape of the XMT-derived profile has a broader reverse zone than the BSE-derived profile, and the XMT profile in the core region is flatter than in the BSE.

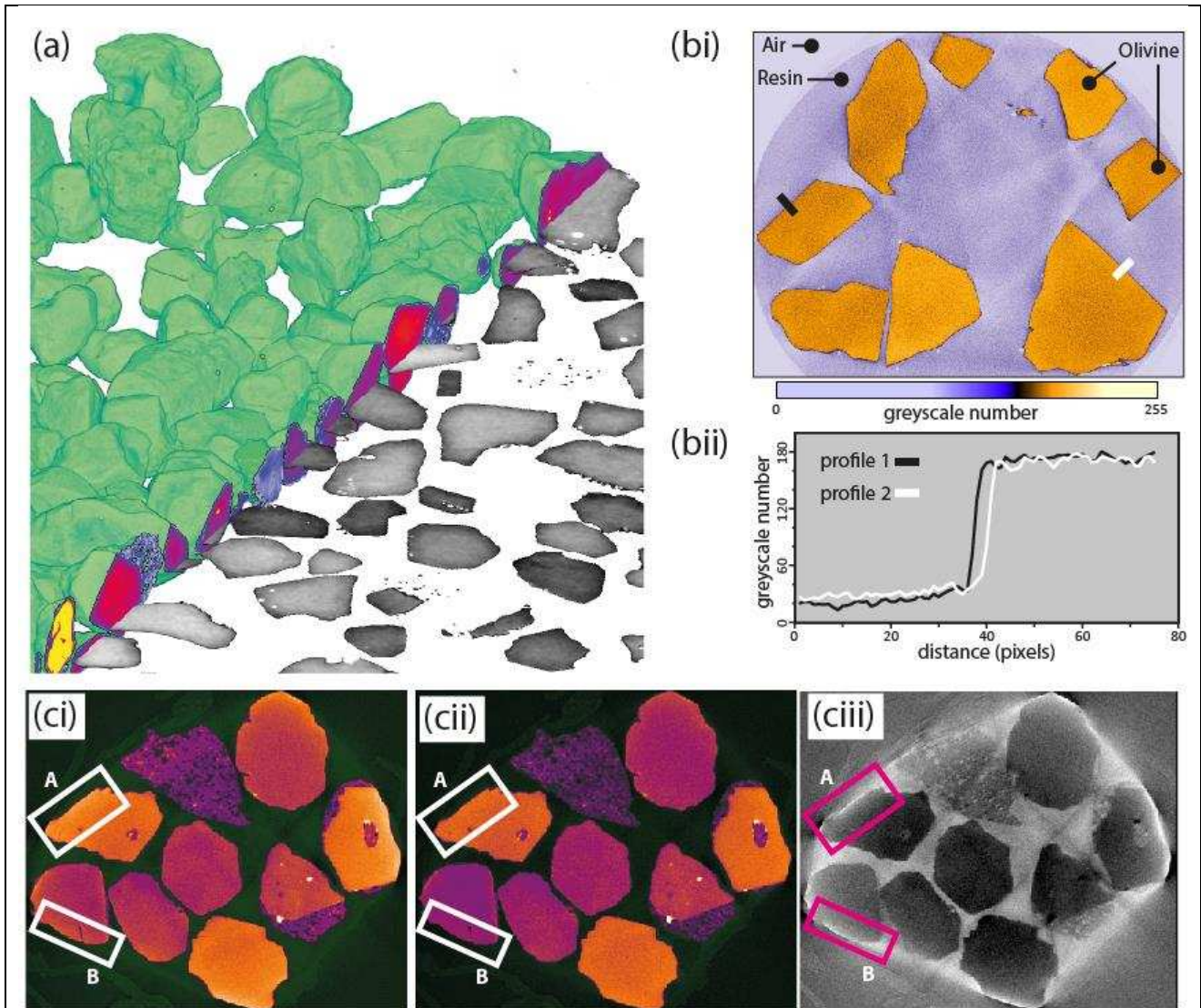


Fig. 4. Olivine attenuation causing beam hardening at margins of grains, and its correction. a) oblique view of olivine grains (volume render, green). Image brightness is shown as red-blue colour map in XZ cutaway and grayscale in XY, the latter approximates the 2D plane that was cut and polished (disc. b) San Carlos olivine shards. According to image brightness, each exhibit internal chemical homogeneity equivalent to that below EPMA uncertainty i) X-ray image after polychromatic beam-characterisation correction to a density value of  $3.34 \text{ g cm}^3$ , ii) profiles demonstrating step function across resin-crystal boundary. c) collection of olivine crystals with inter- and intra-crystal heterogeneity wrapped in plastic film i) before and ii) after correction to a density value of  $3.45 \text{ g cm}^3$ . iii) image cii subtracted from image ci demonstrates the approximately radial beam hardening effect is reduced, and highlights the higher sensitivity to the correction in materials with low attenuation (i.e. the film). Compare box A and B in each image. The brightening is reduced/removed from i to ii; the difference is shown in iii.

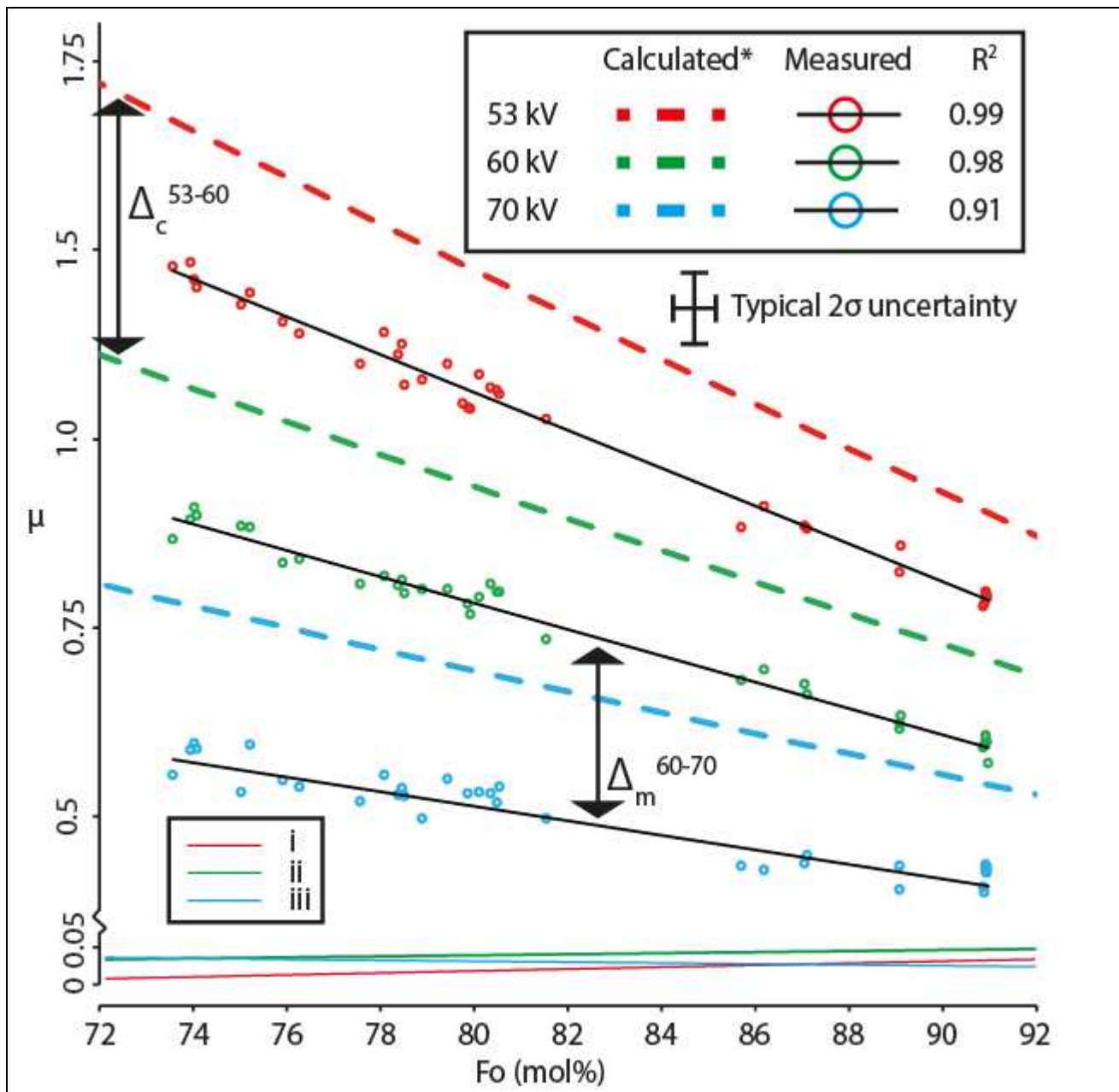


Fig. 5. Calculated vs measured linear attenuation of the olivine solid solution from  $Fo_{73-91}$ . Good linear fits are found in all datasets across  $Fo_{73-91}$ . There are no significant trends in the magnitude of the offset with composition or energy. Greater contrast is observed when using lower energy. At a given  $Fo$  content, the difference between the measured 53 and 60 kV values is the same as the difference between the calculated 52 and 60 kV values, within a range of  $0.025 \mu$  (line i). The same test was applied to 53 and 70 kV data (line ii) and 60 and 70 kV data (line iii), where a total range of  $\sim 0.05 \mu$  was found, which is less than the scatter in any of the measured datasets. No significant trends in the magnitude of the offset with composition or energy are observed.

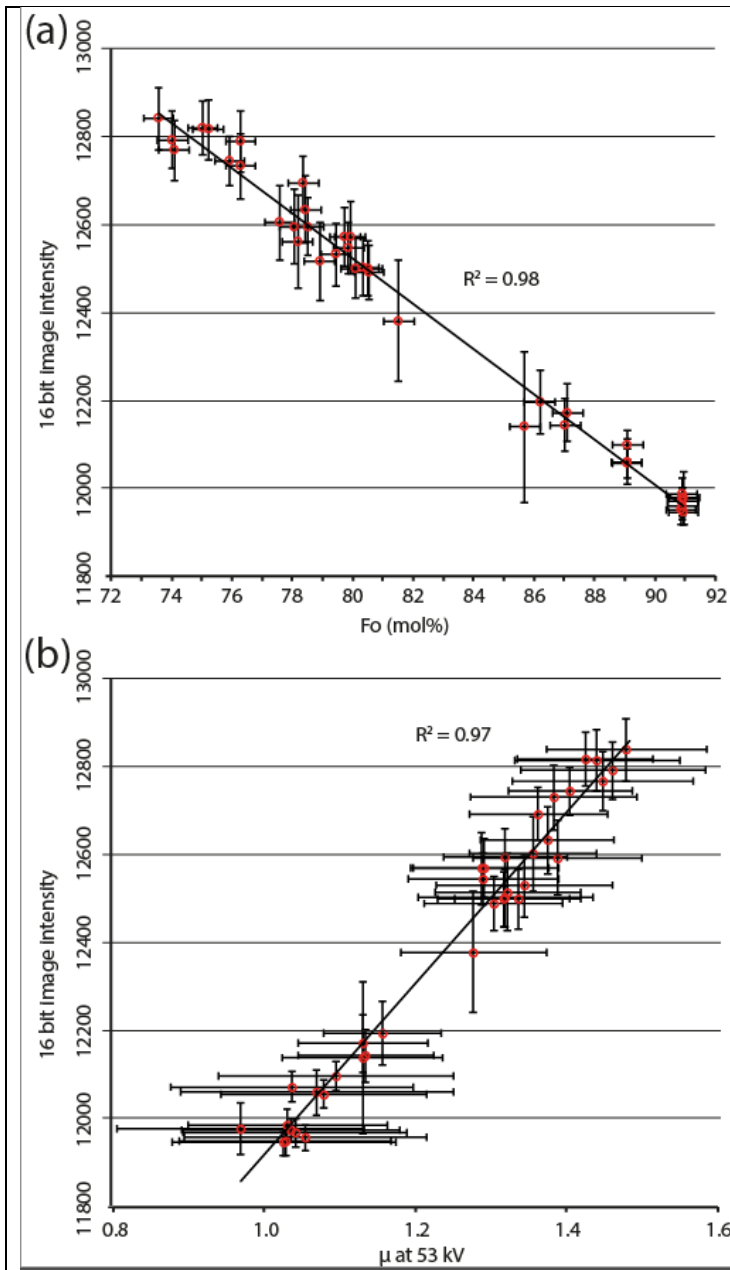


Fig. 6. **Crystal core image brightness from polychromatic X-ray source vs chemical analysis (a) and monochromatic source (b).** Indications of accuracy and usability in a non-synchrotron setting are shown. a) A good fit to a linear regression is observed between polychromatic (laboratory scanner) scan data and EPMA. Point-specific errors reflect the image noise, two standard deviations of pixel values around the mean, at that point (no filtering was performed to generate points on this plot). b) Laboratory scanner data are observed to return higher contrast and better precision than the lowest energy monochromatic (synchrotron source) beam used.

761

762

763

764

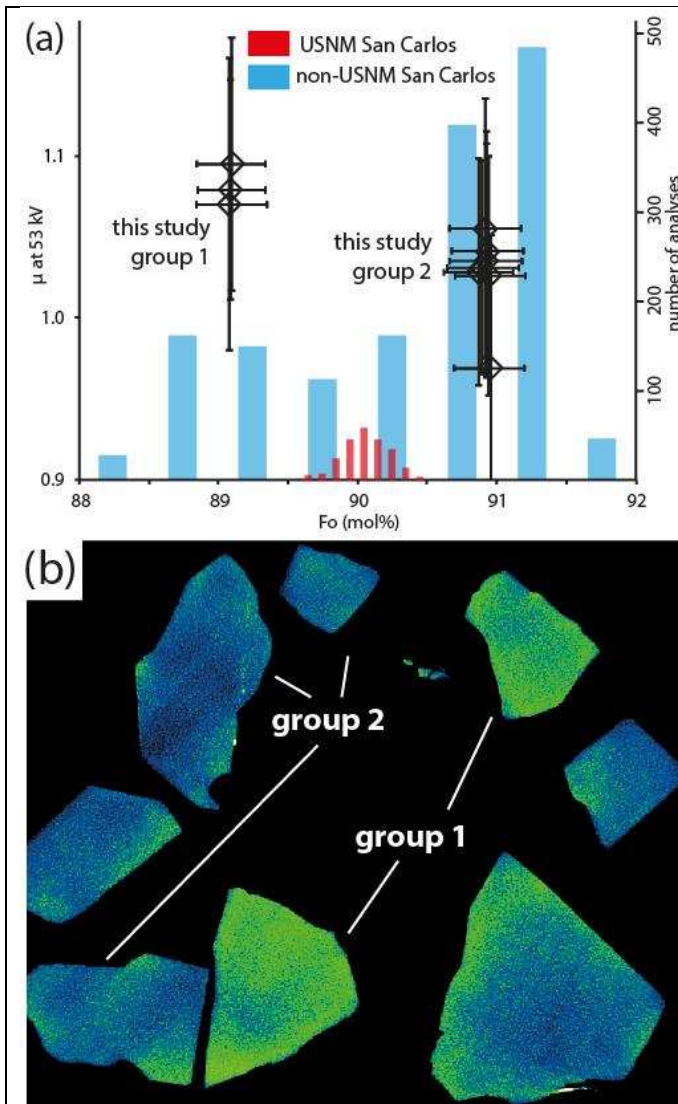


**Fig. 7. Subtle chemical heterogeneity between and within shards of a single crystal of San Carlos forsterite.** a) linear attenuation as measured using monochromatic X-rays vs. EPMA spot analyses show a distinct clustering into Fo<sub>~89</sub> and Fo<sub>~91</sub> groups (1 and 2 respectively). These correspond to the most common compositions of non-USNM San Carlos olivine reported by Fournelle (2011). b) laboratory-source X-ray image. Distinct differences between shards are observed. The image intensity is displayed using an arbitrary colour scheme (green = higher). The range corresponds to ~2 mol % Fo (see a), and is displayed without any filtration to provide an indication of the current signal:noise limit achievable with a modern laboratory scanner and ~1 hour scan time.

765

766

## 767 Supplementary Information

768 Table S1: Example calculations of mass, and linear attenuation coefficients. Mass attenuation  
 769 coefficients (MAC) are calculated using the publically available XCOM database (Berger et al.,  
 770 2016), from which linear attenuation coefficients (LAC) are derived using published values of  
 771 density (Deer et al., 1982).

Photon energy (KeV)	Fa ( $\rho=4.39$ )		Fo ( $\rho=3.271$ )	
	MAC* cm <sup>2</sup> /g	$\mu$	MAC* cm <sup>2</sup> /g	$\mu$
40		2.17 9.51		0.43 1.39
41		2.03 8.9		0.41 1.33
42		1.9 8.34		0.39 1.28
43		1.78 7.83		0.38 1.23
44		1.68 7.36		0.36 1.18
45		1.58 6.94		0.35 1.14
46		1.49 6.55		0.34 1.1
47		1.41 6.19		0.33 1.07
48		1.33 5.86		0.32 1.03
49		1.26 5.55		0.31 1
50		1.2 5.27		0.3 0.98
51		1.14 5.01		0.29 0.95
52		1.09 4.77		0.28 0.93
53		1.04 4.54		0.28 0.9
54		0.99 4.34		0.27 0.88
55		0.94 4.14		0.26 0.86
56		0.9 3.96		0.26 0.85
57		0.86 3.8		0.25 0.83
58		0.83 3.64		0.25 0.81
59		0.8 3.49		0.24 0.8
60		0.76 3.36		0.24 0.78
61		0.74 3.23		0.24 0.77
62		0.71 3.11		0.23 0.76
63		0.68 2.99		0.23 0.75
64		0.66 2.89		0.22 0.73
65		0.63 2.79		0.22 0.72
66		0.61 2.69		0.22 0.71
67		0.59 2.6		0.22 0.71
68		0.57 2.52		0.21 0.7
69		0.56 2.44		0.21 0.69
70		0.54 2.37		0.21 0.68
71		0.52 2.29		0.21 0.67
72		0.51 2.23		0.2 0.66
73		0.49 2.16		0.2 0.66
74		0.48 2.1		0.2 0.65
75		0.47 2.05		0.2 0.64
76		0.45 1.99		0.2 0.64
77		0.44 1.94		0.19 0.63
78		0.43 1.89		0.19 0.63
79		0.42 1.84		0.19 0.62
80		0.41 1.8		0.19 0.62

\*mass attenuation coefficient

773 Table S2: Full results from olivine EPMA. All oxide results reported in wt%. NMNH-111312-44 (Sand Carlos olivine) used as primary reference  
 774 material, USNM-2566 (Springwater Meteorite olivine; see Table 2) and a pre-characterised chip of GEO2 olivine (see Pankhurst et al., 2017), used as a  
 775 secondary reference materials.

SAMPLE	SiO <sub>2</sub>	TiO <sub>2</sub>	Al <sub>2</sub> O <sub>3</sub>	FeO	MnO	MgO	CaO	Cr <sub>2</sub> O <sub>3</sub>	TOTAL	Fo	Fa	Te
FMVD7_1mm_a_ol3	38.38	0.12	0.01	22.78	0.33	38.94	0.24	0.01	100.81	75.02	24.62	
FMVD7_1mm_a_ol3	38.41	0.11	bd	22.75	0.32	38.91	0.24	0.01	100.74	75.04	24.62	
FMVD7_1mm_a_ol4	38.72	0.10	0.01	21.82	0.29	39.80	bd	0.02	100.70	76.24	23.45	
FMVD7_1mm_a_ol4	38.70	0.10	bd	21.65	0.29	39.70	bd	0.02	100.05	76.33	23.35	
FMVD7_1mm_a_ol6	38.20	0.09	0.01	22.67	0.29	38.99	0.18	0.00	100.45	75.16	24.52	
FMVD7_1mm_a_ol6	38.12	0.10	0.02	22.50	0.28	38.94	bd	0.01	99.76	75.29	24.40	
FMVD7_1mm_a_ol7	38.89	0.09	0.01	19.86	0.30	40.71	bd	0.03	99.63	78.26	21.42	
FMVD7_1mm_a_ol7	38.94	0.11	0.01	20.06	0.29	40.72	bd	0.02	99.84	78.10	21.59	
FMVD7_1mm_a_ol8	39.11	0.10	0.02	18.84	0.26	42.52	0.47	0.03	101.34	79.87	19.85	
FMVD7_1mm_a_ol8	39.20	0.09	0.01	18.64	0.26	42.34	bd	0.03	100.25	79.97	19.75	
FMVD7_1mm_a_ol9	39.26	0.10	0.02	18.68	0.26	41.82	bd	0.03	99.72	79.74	19.98	
FMVD7_1mm_a_ol9	39.24	0.10	0.01	18.75	0.25	41.99	bd	0.02	99.97	79.76	19.98	
FMVD7_1mm_a_ol10	38.32	0.10	0.02	21.77	0.29	39.71	0.21	0.00	100.42	76.24	23.44	
FMVD7_1mm_a_ol10	38.37	0.09	0.01	21.68	0.27	39.71	bd	0.01	100.13	76.33	23.38	
FMVD7_1mm_a_ol11	38.78	0.09	0.01	19.97	0.28	41.16	0.43	0.02	100.74	78.37	21.33	
FMVD7_1mm_a_ol11	38.77	0.11	0.01	20.00	0.27	41.22	0.33	0.02	100.73	78.38	21.34	
FMVD7_1mm_a_ol12	39.21	0.10	0.02	18.18	0.24	42.68	bd	0.02	100.04	80.51	19.23	
FMVD7_1mm_a_ol12	39.22	0.10	0.01	18.11	0.24	42.70	0.23	0.03	100.64	80.57	19.18	
FMVD7_1mm_a_ol13	38.94	0.11	0.01	17.92	0.24	42.77	bd	0.03	99.62	80.76	18.98	
FMVD7_1mm_a_ol13	39.09	0.10	0.01	17.96	0.24	42.68	0.28	0.02	100.39	80.70	19.05	
FMVD7_1mm_a_ol15	39.10	0.09	0.01	18.72	0.23	42.10	bd	0.02	99.89	79.84	19.91	
FMVD7_1mm_a_ol15	39.28	0.10	0.01	18.67	0.25	42.17	bd	0.03	100.02	79.89	19.84	
FMVD7_1mm_a_ol16	39.83	0.10	0.03	13.69	0.17	46.29	0.37	0.06	100.55	85.62	14.20	
FMVD7_1mm_a_ol16	39.91	0.07	0.03	13.50	0.18	46.30	bd	0.06	99.89	85.78	14.03	
FMVD7_1mm_a_ol17	38.85	0.10	bd	19.85	0.26	40.99	bd	0.01	99.50	78.42	21.30	
FMVD7_1mm_a_ol17	38.92	0.10	0.01	19.78	0.28	41.08	bd	0.01	99.71	78.49	21.21	
FMVD7_1mm_a_ol18	38.13	0.09	bd	23.51	0.34	38.06	0.77	0.00	100.90	73.98	25.64	
FMVD7_1mm_a_ol18	38.20	0.09	0.00	23.53	0.33	37.99	0.18	0.00	100.33	73.94	25.69	
FMVD7_1mm_a_ol19	38.21	0.10	0.01	23.42	0.34	38.21	bd	0.01	99.73	74.13	25.49	
FMVD7_1mm_a_ol19	38.14	0.08	0.01	23.48	0.35	38.15	0.05	bd	100.24	74.05	25.57	
FMVD7_1mm_a_ol20	37.87	0.09	bd	23.46	0.32	38.11	bd	bd	99.30	74.06	25.58	
FMVD7_1mm_a_ol20	38.12	0.10	0.01	23.49	0.34	38.04	bd	0.00	99.65	73.99	25.63	

FMVD7_1mm_a_ol21	40.14	0.07	0.03	12.28	0.15	47.13	bd	0.06	99.67	87.11	12.74
FMVD7_1mm_a_ol21	40.11	0.07	0.02	12.30	0.17	47.27	0.21	0.05	100.20	87.11	12.71
FMVD7_1mm_a_ol22	39.34	0.09	0.02	17.26	0.23	43.33	bd	0.03	100.02	81.54	18.22
FMVD7_1mm_a_ol22	39.41	0.10	0.01	17.25	0.24	43.31	bd	0.02	99.87	81.53	18.21
FMVD7_1mm_a_ol23	40.04	0.09	0.02	13.01	0.17	46.22	bd	0.06	99.15	86.21	13.61
FMVD7_1mm_a_ol23	40.16	0.07	0.02	13.08	0.16	46.34	bd	0.06	99.21	86.18	13.65
FMVD7_1mm_a_ol24	38.72	0.10	0.01	20.55	0.29	40.44	bd	0.02	99.66	77.57	22.12
FMVD7_1mm_a_ol24	38.68	0.09	0.01	20.53	0.29	40.46	bd	0.01	99.82	77.59	22.09
FMVD7_1mm_a_ol25	38.97	0.09	0.00	18.24	0.24	42.48	bd	0.02	99.77	80.38	19.36
FMVD7_1mm_a_ol25	38.97	0.08	0.01	18.30	0.25	42.51	bd	0.01	99.56	80.33	19.40
FMVD7_1mm_a_ol26	39.06	0.08	0.02	18.12	0.24	42.43	bd	0.02	99.56	80.47	19.27
FMVD7_1mm_a_ol26	39.00	0.09	0.01	18.05	0.26	42.46	bd	0.02	99.39	80.52	19.20
FMVD7_1mm_a_ol27	39.33	0.08	0.02	15.61	0.21	44.42	bd	0.04	99.32	83.35	16.43
FMVD7_1mm_a_ol27	39.54	0.09	0.02	15.73	0.22	44.41	bd	0.06	99.51	83.23	16.53
FMVD7_1mm_a_ol28	40.18	0.07	0.03	12.33	0.16	47.12	bd	0.06	99.29	87.05	12.78
FMVD7_1mm_a_ol28	40.30	0.07	0.03	12.33	0.17	47.07	bd	0.06	99.60	87.03	12.79
FMVD7_1mm_a_ol29	38.95	0.08	0.01	19.89	0.27	41.20	bd	0.01	100.09	78.46	21.25
FMVD7_1mm_a_ol29	38.95	0.10	0.02	19.76	0.28	41.27	0.43	0.01	100.82	78.59	21.10
FMVD7_1mm_a_ol30	39.13	0.09	0.01	19.05	0.27	41.83	bd	0.02	99.81	79.42	20.29
FMVD7_1mm_a_ol30	38.97	0.08	0.02	19.00	0.26	41.84	bd	0.03	100.18	79.48	20.24
FMVD7_1mm_a_ol31	38.69	0.09	0.02	20.18	0.29	40.93	0.47	0.02	100.69	78.09	21.60
FMVD7_1mm_a_ol31	38.71	0.10	0.02	20.18	0.29	40.88	bd	0.01	99.98	78.07	21.62
FMVD7_1mm_a_ol32	38.48	0.10	0.00	22.00	0.31	39.33	bd	0.01	99.76	75.86	23.80
FMVD7_1mm_a_ol32	38.55	0.10	0.02	21.90	0.31	39.41	0.08	0.00	100.37	75.98	23.69
FMVD7_1mm_a_ol33	37.99	0.07	0.01	23.82	0.33	37.84	bd	0.00	99.56	73.64	26.00
FMVD7_1mm_a_ol33	37.86	0.09	0.00	23.95	0.31	37.78	bd	0.02	99.97	73.51	26.14
FMVD7_1mm_a_ol34	38.74	0.09	0.01	19.50	0.27	41.50	0.01	0.01	100.11	78.91	20.80
FMVD7_1mm_a_ol34	38.71	0.09	0.01	19.50	0.28	41.46	0.62	0.02	100.69	78.89	20.81
FMVD7_1mm_a_ol35	39.09	0.09	0.02	18.45	0.26	42.20	bd	0.02	99.44	80.09	19.64
FMVD7_1mm_a_ol35	39.04	0.10	0.02	18.48	0.25	42.33	0.33	0.03	100.58	80.11	19.62
RP_1	29.62	0.11	bd	66.52	2.55	0.01	0.03	0.00	98.81	96.23	3.74
RP_1r	29.63	0.13	bd	66.59	2.56	-0.01	bd	0.00	98.58	96.27	3.75
RP_2	29.64	0.12	bd	66.46	2.59	0.00	bd	0.00	98.40	96.19	3.80
RP_2r	29.49	0.10	bd	66.34	2.60	0.02	0.19	0.01	98.71	96.14	3.82
RP_3	29.59	0.12	bd	65.90	2.55	-0.01	bd	0.00	97.93	96.25	3.78
RP_3r	29.73	0.13	bd	66.27	2.55	0.01	bd	0.01	98.56	96.22	3.75
RP_4	29.64	0.12	bd	66.23	2.54	-0.01	bd	bd	98.08	96.30	3.73

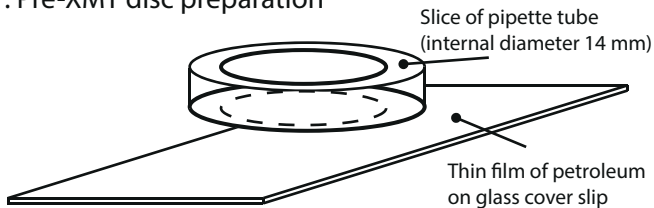


RP_4r	29.71	0.12	bd	66.57	2.57	0.01	bd	0.00	98.56		96.20	3.77
RP_5	29.60	0.11	bd	66.31	2.57	0.01	bd	0.00	98.17		96.21	3.77
RP_5r	29.57	0.11	bd	66.35	2.54	bd	bd	bd	98.09		96.32	3.73
RP_6	29.76	0.12	bd	66.62	2.54	0.01	bd	0.00	98.93		96.26	3.72
RP_6r	29.79	0.09	bd	66.86	2.53	0.02	bd	0.00	98.72		96.26	3.70
RP_8	29.74	0.10	bd	66.55	2.53	0.01	bd	0.00	98.39		96.27	3.71
RP_8r	29.71	0.12	bd	66.42	2.54	0.01	bd	0.00	97.95		96.25	3.73
RP_9	29.55	0.11	bd	66.14	2.56	bd	0.05	0.00	98.37		96.22	3.77
RP_9r	29.64	0.11	bd	66.21	2.58	bd	bd	bd	98.41		96.22	3.80
RP_10	29.75	0.12	bd	66.42	2.53	0.01	bd	bd	98.58		96.25	3.72
RP_10r	29.75	0.12	bd	66.61	2.55	0.00	0.08	bd	99.07		96.27	3.73
RP_11	29.77	0.12	bd	66.62	2.54	0.03	bd	bd	98.97		96.21	3.72
RP_11r	29.76	0.13	bd	66.41	2.56	0.00	bd	0.00	98.29		96.25	3.75
RP_12	29.79	0.12	bd	66.33	2.53	0.01	bd	0.00	98.64		96.26	3.72
RP_12r	29.79	0.13	bd	66.37	2.57	bd	bd	0.00	98.80		96.26	3.78
RP_13	29.64	0.12	bd	66.25	2.54	0.01	bd	0.01	98.29		96.24	3.74
RP_13r	29.62	0.11	bd	66.15	2.56	0.01	bd	0.01	97.91		96.22	3.77
RP_14	29.79	0.13	bd	66.62	2.55	0.00	0.17	0.00	99.23		96.27	3.74
RP_14r	29.74	0.13	bd	66.64	2.49	0.01	0.17	0.01	99.16		96.32	3.64
RP_15	29.69	0.13	bd	66.35	2.59	bd	bd	0.00	98.63		96.24	3.81
RP_15r	29.79	0.13	bd	66.43	2.58	0.02	0.19	0.00	99.08		96.18	3.78
SC_1	41.20	0.08	bd	8.82	0.13	50.33	0.12	0.03	100.70	90.93	8.94	
SC_1r	41.13	0.08	bd	8.82	0.13	50.48	bd	0.03	100.32	90.96	8.91	
SC_1r2	40.98	0.07	bd	8.83	0.13	50.58	bd	0.02	100.39	90.95	8.91	
SC_2	41.05	0.08	bd	8.87	0.14	50.42	bd	0.02	100.05	90.89	8.97	
SC_2r	40.94	0.08	bd	8.83	0.14	50.52	bd	0.08	100.23	90.94	8.91	
SC_2r2	40.95	0.08	bd	8.85	0.13	50.55	bd	0.02	100.15	90.94	8.93	
SC_3	41.17	0.09	bd	8.88	0.12	50.61	bd	0.02	100.54	90.92	8.95	
SC_3r	41.19	0.09	bd	8.86	0.14	50.56	0.06	0.02	100.91	90.92	8.94	
SC_3r2	41.16	0.09	bd	8.87	0.12	50.47	bd	0.01	100.61	90.91	8.97	
SC_4	40.70	0.08	bd	10.55	0.16	49.16	bd	0.01	100.26	89.11	10.73	
SC_4r	41.19	0.10	bd	10.49	0.15	48.35	bd	0.01	100.29	89.01	10.83	
SC_4r2	40.85	0.08	bd	10.48	0.15	49.08	bd	0.02	100.53	89.17	10.68	
SC_5	41.24	0.08	bd	8.83	0.13	50.38	bd	0.02	100.13	90.92	8.94	
SC_5r	41.26	0.08	bd	8.87	0.12	50.29	bd	0.02	100.20	90.89	8.99	
SC_5r2	41.16	0.09	bd	8.91	0.14	50.53	0.00	0.03	100.85	90.87	8.99	
SC_6	41.03	0.10	bd	10.53	0.15	49.08	bd	0.02	100.60	89.12	10.72	

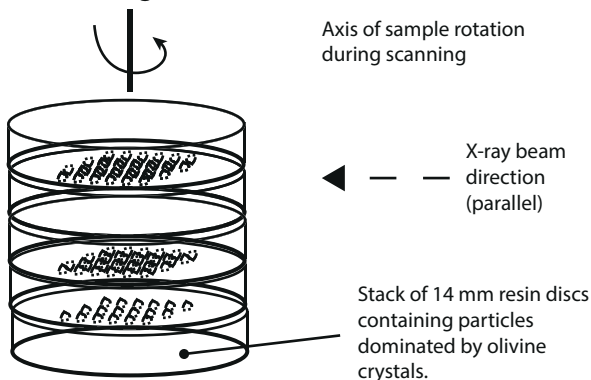
SC_6r	40.91	0.09	bd	10.59	0.15	49.08	bd	0.03	100.53	89.07	10.78
SC_6r2	40.97	0.09	bd	10.62	0.15	49.09	0.12	0.02	101.06	89.04	10.80
SC_7	41.18	0.08	bd	8.81	0.13	50.63	bd	0.02	100.81	90.99	8.88
SC_7r	41.18	0.08	bd	8.81	0.13	50.49	0.00	0.02	100.70	90.96	8.90
SC_7r2	41.22	0.09	bd	8.87	0.12	50.55	bd	0.04	100.65	90.92	8.95
SC_9	41.22	0.09	bd	8.87	0.14	50.54	bd	0.02	100.58	90.91	8.96
SC_9r	41.14	0.09	bd	8.85	0.14	50.49	bd	0.02	100.43	90.92	8.94
SC_9r2	41.22	0.08	bd	8.81	0.12	50.38	bd	0.03	100.24	90.95	8.92
SC_10	41.04	0.09	bd	10.59	0.15	49.07	bd	0.01	100.31	89.06	10.79
SC_10r	40.84	0.08	bd	10.55	0.16	49.16	0.17	0.01	100.97	89.10	10.73
SC_10r2	40.82	0.09	bd	10.52	0.16	48.95	bd	0.01	100.15	89.09	10.74
SC_11	41.19	0.09	bd	8.93	0.12	50.47	bd	0.01	100.44	90.86	9.02
SC_11r	41.22	0.07	bd	8.92	0.14	50.36	0.08	0.02	100.80	90.83	9.03
SC_11r2	41.08	0.09	bd	8.83	0.13	50.26	bd	0.02	100.16	90.91	8.96

776 r denotes repeat spot analysis, <10 μm from the original. r2 is a second repeat, also <10 μm from the original

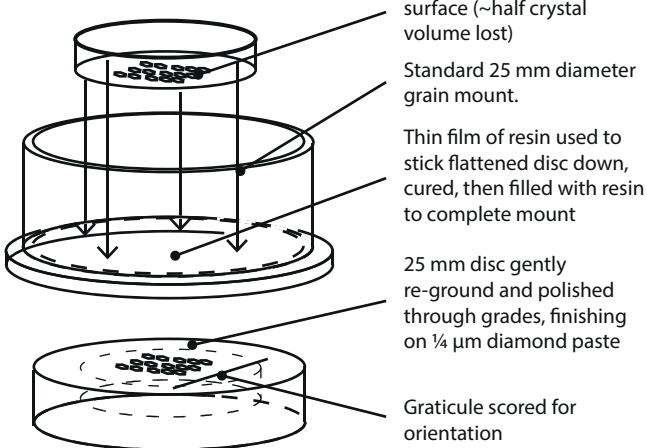
## 1. Pre-XMT disc preparation

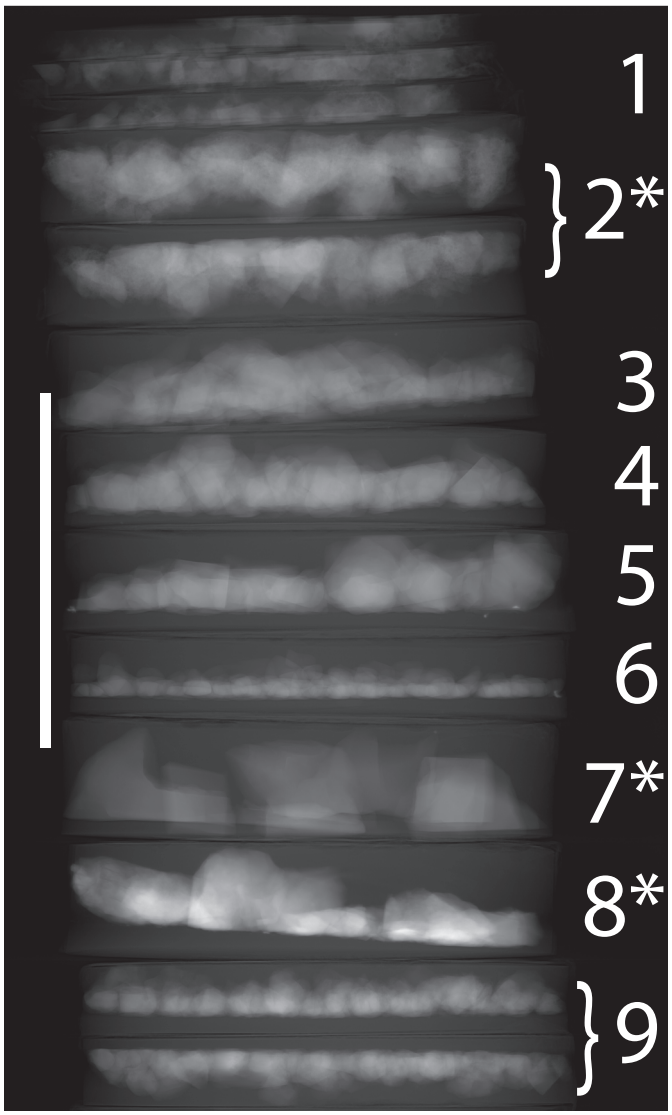


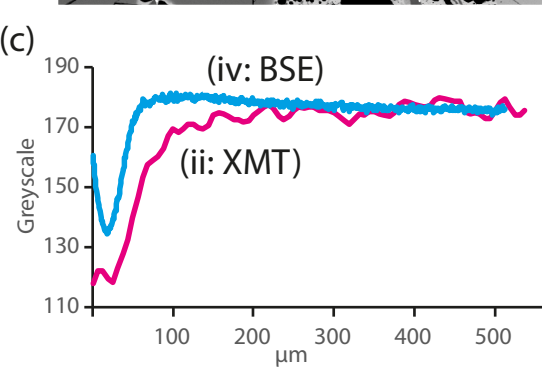
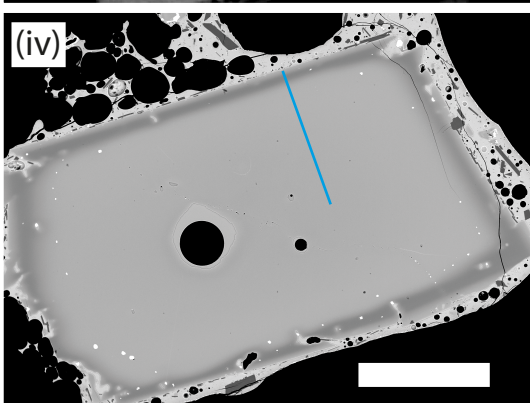
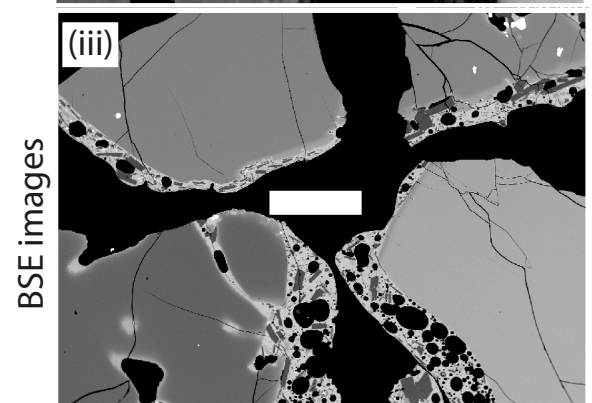
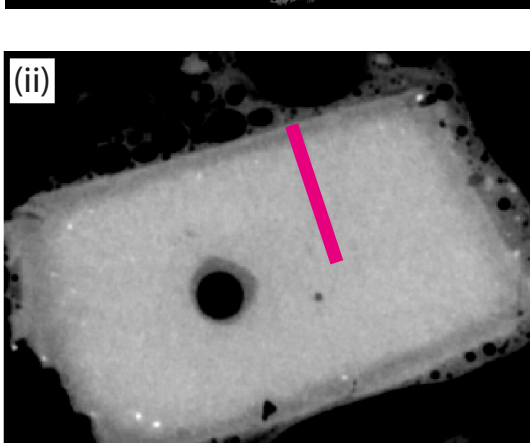
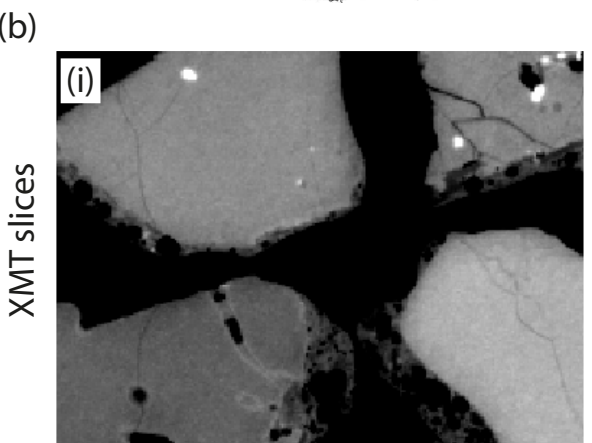
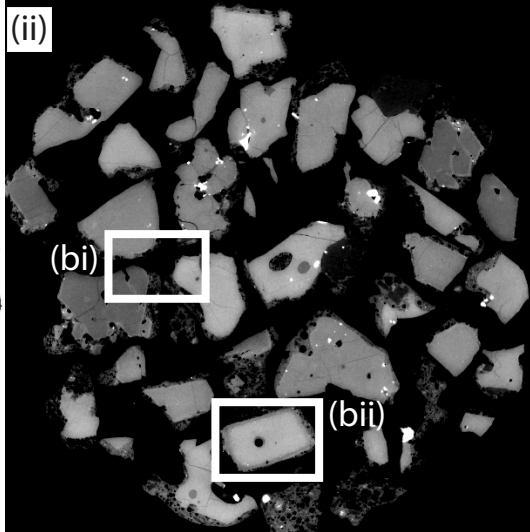
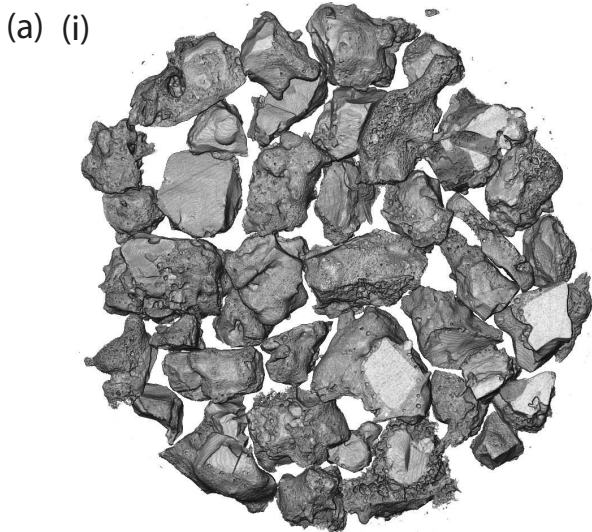
## 2. XMT scanning

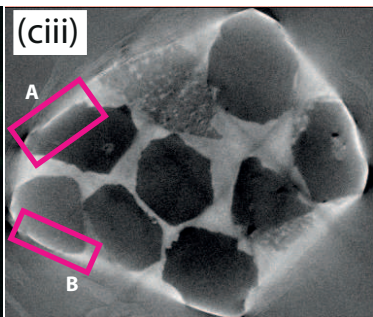
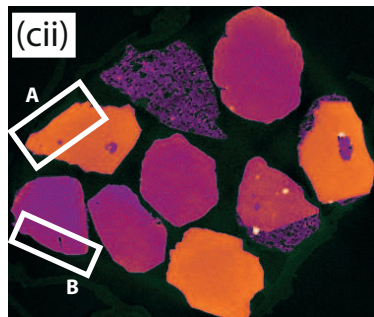
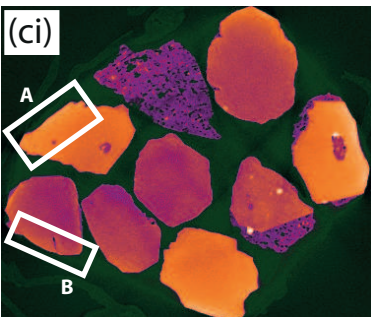
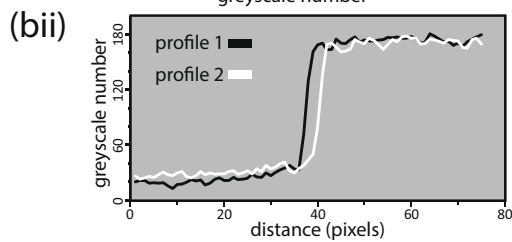
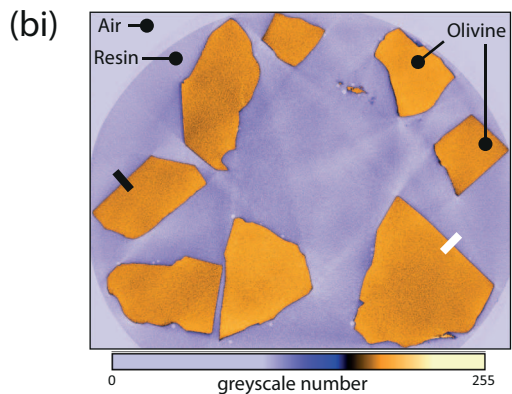
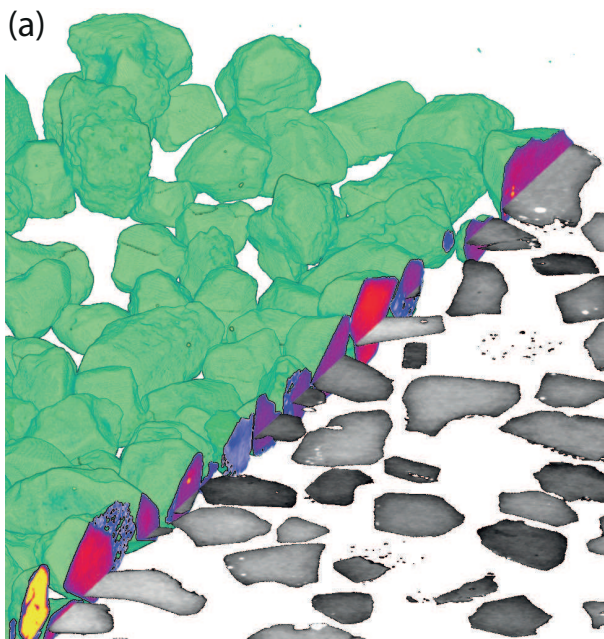


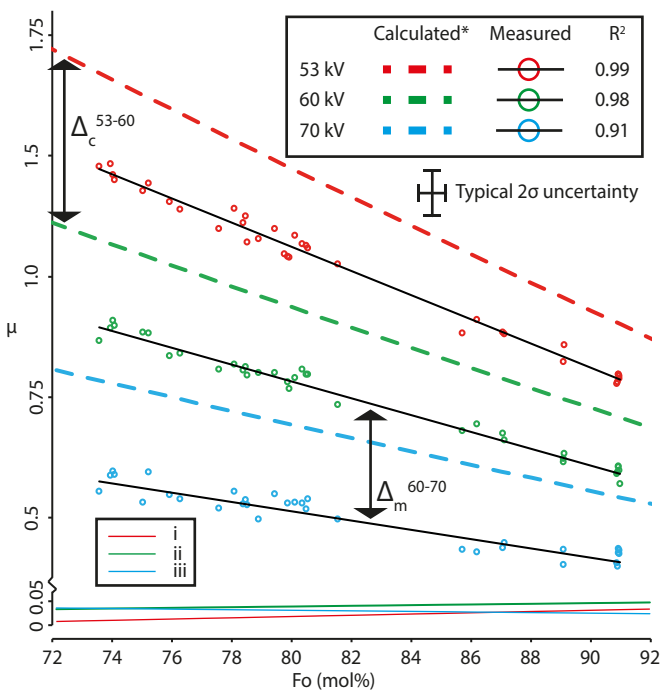
## 3. Pre-EPMA preparation

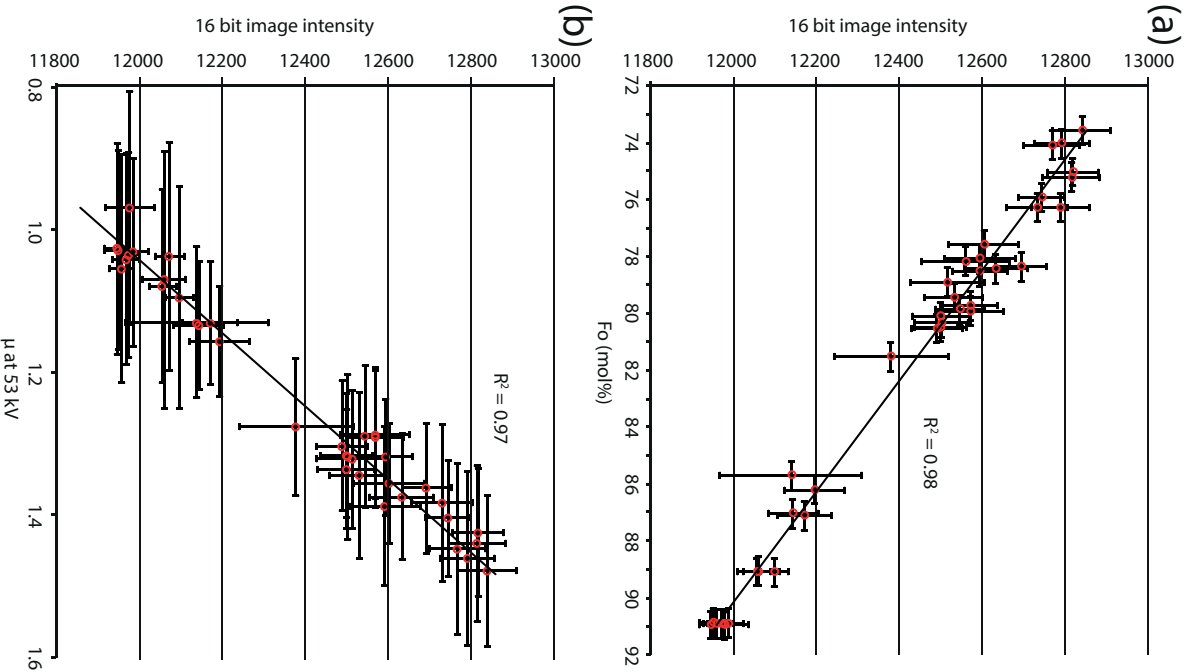




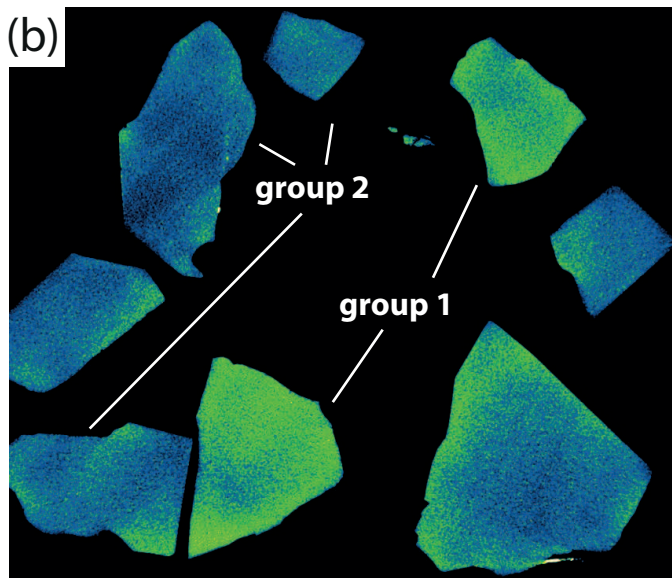
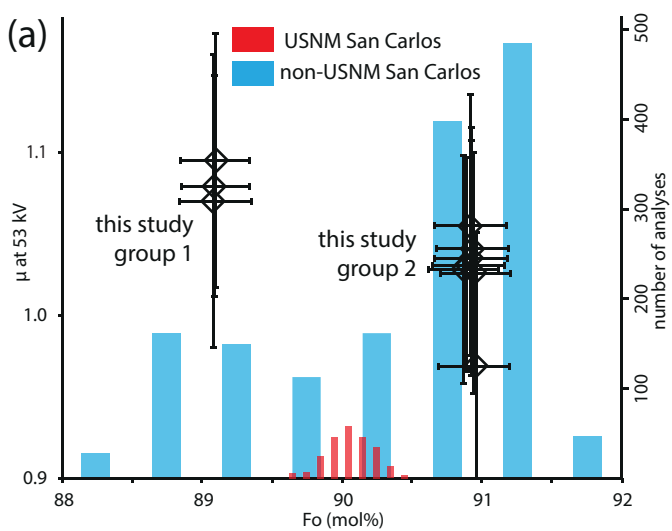


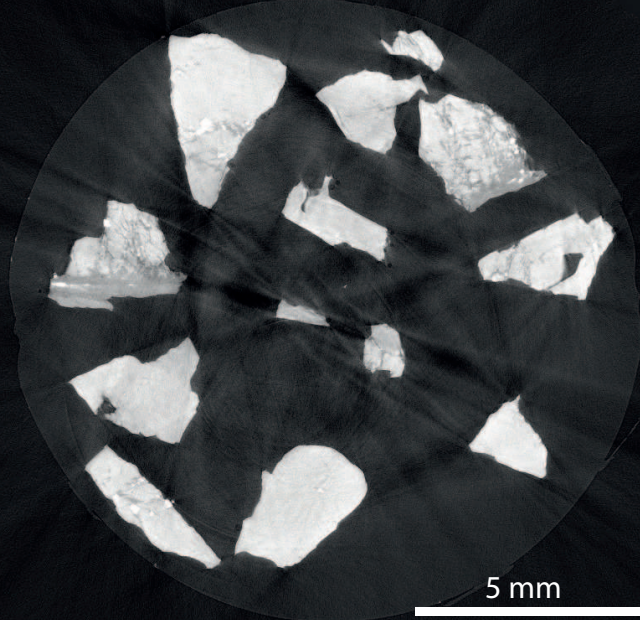












5 mm